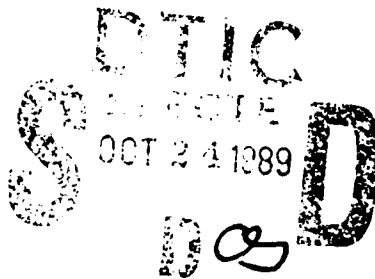WRDC-TR-89-2082

AD-A213 575

HIGH POWER DENSITY SPRAY COOLING

Donald E. Tilton
Martin R. Pais
Louis C. Chow

University of Kentucky
Department of Mechanical Engineering
Lexington, KY 40506-0046

July 1989

Interim Report for Period July 1987 — August 1988
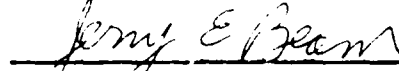
NOTICE

When Government drawings, specifications, or other data are used for any purpose other than in connection with a definitely Government-related procurement, the United States Government incurs no responsibility or any obligation whatsoever. The fact that the government may have formulated or in any way supplied the said drawings, specifications, or other data, is not to be regarded by implication, or otherwise in any manner construed, as licensing the holder, or any other person or corporation; or as conveying any rights or permission to manufacture, use, or sell any patented invention that may in any way be related thereto.

This report is releasable to the National Technical Information Service (NTIS). At NTIS, it will be available to the general public, including foreign nations.

This technical report has been reviewed and is approved for publication.
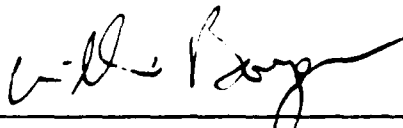
MICHEAL J. MORGAN
Power Technology Branch
Aerospace Power Division
Aero Propulsion and Power Laboratory

JERRY E. BEAM
Power Technology Branch
Aerospace Power Division
Aero Propulsion and Power Laboratory

FOR THE COMMANDER

WILLIAM U. BORGER
Chief, Aerospace Power Division
Aero Propulsion & Power Laboratory

If your address has changed, if you wish to be removed from our mailing list, or if the addressee is no longer employed by your organization please notify WRDC/POOS, WPAFB, OH 45433-6563 to help us maintain a current mailing list.

Copies of this report should not be returned unless return is required by security considerations, contractual obligations, or notice on a specific document.

REPORT DOCUMENTATION PAGE

Form Approved
OMB No. 0704-0188

1a. REPORT SECURITY CLASSIFICATION	1b. RESTRICTIVE MARKINGS
Unclassified	

2a. SECURITY CLASSIFICATION AUTHORITY	3. DISTRIBUTION/AVAILABILITY OF REPORT
	Approved for public release
2b. DECLASSIFICATION/DOWNGRADING SCHEDULE	Distribution is unlimited

4. PERFORMING ORGANIZATION REPORT NUMBER(S)	5. MONITORING ORGANIZATION REPORT NUMBER(S)
UK-ME-88-07	WRDC-TR-89-2082

6a. NAME OF PERFORMING ORGANIZATION	6b. OFFICE SYMBOL (If applicable)	7a. NAME OF MONITORING ORGANIZATION
University of Kentucky		Aero Propulsion and Power Laboratory (WRDC/POOS) Wright Research and Development Center, AFSC

6c. ADDRESS (City, State, and ZIP Code)	7b. ADDRESS (City, State, and ZIP Code)
Department of Mechanical Engineering Lexington, KY 40506-0046	Wright-Patterson AFB, OH 45433-6563

8a. NAME OF FUNDING/SPONSORING ORGANIZATION	8b. OFFICE SYMBOL (If applicable)	9. PROCUREMENT INSTRUMENT IDENTIFICATION NUMBER
		F33615-87-C-2777

8c. ADDRESS (City, State, and ZIP Code)	10. SOURCE OF FUNDING NUMBERS			
	PROGRAM ELEMENT NO.	PROJECT NO.	TASK NO	WORK UNIT ACCESSION NO.

11. TITLE (Include Security Classification)

High Power Density Spray Cooling

12. PERSONAL AUTHOR(S)

Tilton, Donald E.; Pais, Martin R.; Chow, Louis C.

13a. TYPE OF REPORT	13b. TIME COVERED	14. DATE OF REPORT (Year, Month, Day)	15. PAGE COUNT
Interim	FROM 87 JUL TO 88 AUG	July 1989	62

16. SUPPLEMENTARY NOTATION

17. COSATI CODES			18. SUBJECT TERMS (Continue on reverse if necessary and identify by block number)
FIELD	GROUP	SUB-GROUP	Evaporative cooling, spray cooling, high heat flux, critical heat flux

19. ABSTRACT (Continue on reverse if necessary and identify by block number)

The research reported describes experimental and theoretical investigations of high power density evaporative spray cooling. Preliminary experiments demonstrating heat fluxes greater than 1,000 W/sq cm were conducted. Extensive laser phase Doppler measurements of spray characteristics were also taken. These measurements provided valuable insight into the heat transfer process. An in-depth analysis was conducted to determine the mechanisms responsible for critical heat flux. Theoretical modeling was also conducted to determine the most desirable heat transfer conditions. After analysis of these results, an improved experimental apparatus was designed and fabricated. The new apparatus provided greater experimental control and improved accuracy. New tests were conducted in which the critical heat flux was increased, and the heat transfer efficiency was greatly improved. These results are compared to those of previous researchers, and indicate substantial improvement.

20. DISTRIBUTION/AVAILABILITY OF ABSTRACT	21. ABSTRACT SECURITY CLASSIFICATION
☒ UNCLASSIFIED/UNLIMITED ☐ SAME AS RPT. ☐ DTIC USERS	Unclassified

22a. NAME OF RESPONSIBLE INDIVIDUAL	22b. TELEPHONE (Include Area Code)	22c. OFFICE SYMBOL
Dr. Jerry E. Beam	(513) 255-6241	WRDC/POOS

DD Form 1473, JUN 86   Previous editions are obsolete.   SECURITY CLASSIFICATION OF THIS PAGE

FOREWORD

The research reported is part of a continuing investigation of high power density evaporative cooling. The research is sponsored by Aero Propulsion and Power Laboratory. Dr. Jerry E. Beam of the Nuclear/Thermal Technology group was the contract monitor during this reporting period. Mr. Micheal Morgan is the current technical monitor. The guidance and inspiration of Dr. Tom Mahefkey are also greatly appreciated.

The research was conducted primarily in the Heat Transfer Laboratory at the University of Kentucky. The laser phase Doppler measurements of the spray characteristics described in the report were taken at the Aero Propulsion and Power Laboratories Combustion Research Facility with the assistance of Mr. Gary Switzer and Dr. Mel Roquemore.

TABLE OF CONTENTS

LIST OF ILLUSTRATIONS

LIST OF TABLES

NOMENCLATURE

A	Area
d	Droplet diameter
D	Hemispherical droplet diameter
h_{fg}	Latent heat of vaporization
k	Thermal conductivity
l	Length
q	Heat flux
r	Droplet radius, radial coordinate
r_d	Spread droplet radius
R	Unit cell radius
t	time
t_{res}	Residence time of droplet on surface
T	Temperature
u	Vapor escape velocity
v	Droplet velocity
v_o	Initial droplet velocity
V	Thermocouple voltage
w	Uncertainty variable
We	Weber number
x	Axial coordinate
α	Thermal diffusivity
δ	Dimensionless droplet diameter
ϕ	Dimensionless heat flux
η	Dimensionless radial coordinate
λ	Dimensionless axial coordinate
τ	Dimensionless time coordinate
θ	Dimensionless temperature
ϵ	Percent surface saturation
ρ	Density
μ	Viscosity
σ	Surface tension
γ	Dimensionless droplet volume

I. INTRODUCTION

High power density spray cooling has been receiving a considerable amount of attention. The development of future high power spacecraft thermal management systems may require very high heat fluxes to be removed from surfaces maintained at low temperature. The surface temperature must be low to protect the integrity of the VLSI electronic components. At the same time, the waste heat must be rejected to space by radiation. Since radiation depends on the temperature to the fourth power, the temperature of the coolant must be as high as possible to keep radiator size and weight requirements at an acceptable level. Therefore, a very efficient cooling method is imperative.

Spray evaporative cooling has been demonstrated to be a viable method to remove very high heat flux values from surfaces with low superheats (surface temperature minus fluid saturation temperature). In fact, the efficiency of spray cooling exceeds that found in conventional pool boiling by an order of magnitude.

This report describes the research effort directed towards developing a fundamental understanding of the spray cooling process. The research effort is divided into three sections containing preliminary experimental results, analysis and theory, and new experiments performed with an improved apparatus.

II. OBJECTIVE OF THE RESEARCH EFFORT

The objective of the research effort is to develop a fundamental
understanding of the evaporative spray cooling process through
experimentation, measurement and analysis of the spray characteristics.
Once we determine how the spray characteristics effect the heat transfer
process, we can use this information to improve heat transfer efficiency
and increase the maximum heat flux. The main hypotheses are (1) that
the droplet/vapor interaction is responsible for transition to film
boiling, and (2) that the liquid distribution on the surface resulting
from a given set of spray conditions affects the heat transfer
efficiency.

III. BACKGROUND

Current heat transfer enhancement research has been directed towards phase change processes. This is because the relatively large latent heat can be extracted with only a few degrees superheat. Of the various types of phase change heat transfer, spray cooling holds the greatest promise for large increases in heat transfer efficiency and maximum heat flux.

Analysis of previously published data for experimentation where surfaces are spray cooled with water in air at one atmosphere indicates that the heat transfer is highly dependent on the spray characteristics. Toda performed experiments which showed maximum heat flux values of 200 to 250 W/cm^2 consistently occurred at a surface superheat (surface temperature minus fluid saturation temperature) between 30 and 60 ^0C [1]. Eastman and Ernst demonstrated that heat fluxes of up to 2,000 W/cm^2 can be removed from a surface maintained at 300 ^0C [2]. Bonacina et al. investigated the low heat flux range using very low percentages of surface saturation [3]. Heat transfer coefficients for this research ranged from 1.5 to 15 W/cm K with variation in droplet diameter and percentage of surface saturation. The heat transfer results show a wide variation with spray characteristics. This indicates that extensive testing is necessary to quantify the effects of the spray characteristics and develop a fundamental understanding of spray evaporative cooling.

To understand spray cooling completely, we need to examine the phase change process which occurs at the curved liquid/vapor interface. References [4-12] provide an in-depth analysis of this process from a thermodynamic and mechanical equilibrium standpoint. The main conclusion is that for low superheats, evaporative heat transfer can be enhanced by using flat liquid films of minimum thickness.

A study of the theory of pool boiling is useful for appreciating the inter-relationship of factors upon which spray cooling heat transfer depends. The effect of the hydrodynamic instabilities, which prevent liquid/solid contact, resulting in reduced heat transfer efficiency, is a particularly crucial factor. This occurs when the critical heat flux

3

(CHF), which is the highest heat flux at which the surface remains wetted, is past. A similar effect resulting from the droplet/vapor interaction can be anticipated in spray cooling. If droplets are small and their velocities are low, they may become entrained in the escaping vapor and never reach the surface. Conversely, if they are too large and fast, their kinetic energy cannot be absorbed by the impact with the surface, causing rebound and splashing. Also, liquid can be expelled from the surface by nucleating bubbles within the thin film. All of these effects will result in insufficient liquid supply to the surface which causes a transition to a nonwetting surface condition. This is analogous to the Helmholtz instability which causes the transition in pool boiling. Another factor which effects the pool boiling process significantly is the surface roughness and wetting characteristics. Just as in pool boiling, rough surfaces which have good wetting characteristics are expected to enhance the heat transfer for spray cooling. References [13-15] represent a few examples of the numerous investigations into the theory of pool boiling, the theory of nucleation, and the solid/liquid/vapor relationship of boiling from which these conclusions are drawn.

This research effort is directed towards maximizing/enhancing the critical heat flux, and concurrently reducing the superheat. The hydrodynamic instability which limits liquid supply in the case of pool boiling can be precluded for spray cooling if the spray characteristics are properly chosen to avoid entrainment and rebound. This is why the CHF for spray cooling can be so much higher than that for pool boiling.

In contrast to boiling, spray cooling involves thin film evaporation and nucleation. In thin film evaporation, the liquid molecules escape directly into the vapor/ambient at the free surface. From phase change thermodynamics, the inception of vapor bubbles on the hot surface is partially dependent on the liquid/solid boundary conditions, for example, on the availability of nucleation sites. The heat transfer depends on the surface roughness conditions and the liquid film thickness. For very thin films on smooth surfaces, evaporation predominates. For thick films on rough surfaces, nucleation predominates. In many cases both effects are very important. However, the most efficient heat transfer occurs when ultra-thin, uniform films

4

exist. Therefore, the goal of this research is to provide a uniform thin film of liquid on the surface so the heat flux can be maximized with a minimum superheat.

IV. PRELIMINARY EXPERIMENTATION

To begin the investigation into spray cooling, we performed
preliminary experimentation to understand the spray cooling process and
identify the important factors governing the process. This section
describes the experimental setup and the results obtained.

4.1 EXPERIMENTAL DESCRIPTION

The preliminary high power density evaporative cooling test
apparatus is shown in Figure 4.1.1. The heater block is a solid copper
cylinder 10 cm in diameter. Six 1,000-Watt cartridge heaters are
inserted into the heater block. These heaters are controlled with a
rheostat so that a variable power input may be obtained. The test
surface is clamped to the heater block which is supported in a plexiglas
box and surrounded with ceramic fiber insulation. A machinable ceramic
seal and stainless steel cover are used to protect the insulation from
the spray and ensure that heat removal occurred only by evaporation from
the exposed test surface. This apparatus is capable of supplying up to
1,200 W/cm^2 to a 2.0-cm-diameter smooth copper surface.

During testing, the temperature gradient just below the sprayed
surface is measured by six thermocouples. Three thermocouples measure
the temperature gradient at the centerline. The other three
thermocouples measure the temperature gradient at a radial distance of
0.5 cm. A data logger records the temperature measurements, calculates
the heat flux and the surface temperature.

A variable-speed magnetic drive gear pump controls the nozzle
pressure accurately at the desired pressure. The pressure and flow rate
are measured. Four different nozzles ranging from 0.51 to 0.76 mm in
orifice diameter were used. The droplet diameters, velocities, and flow
rates for the experiments performed are presented in the following
section. The distance between the nozzle and the test surface can be
varied but was left at 1.9 cm for the cases presented here.
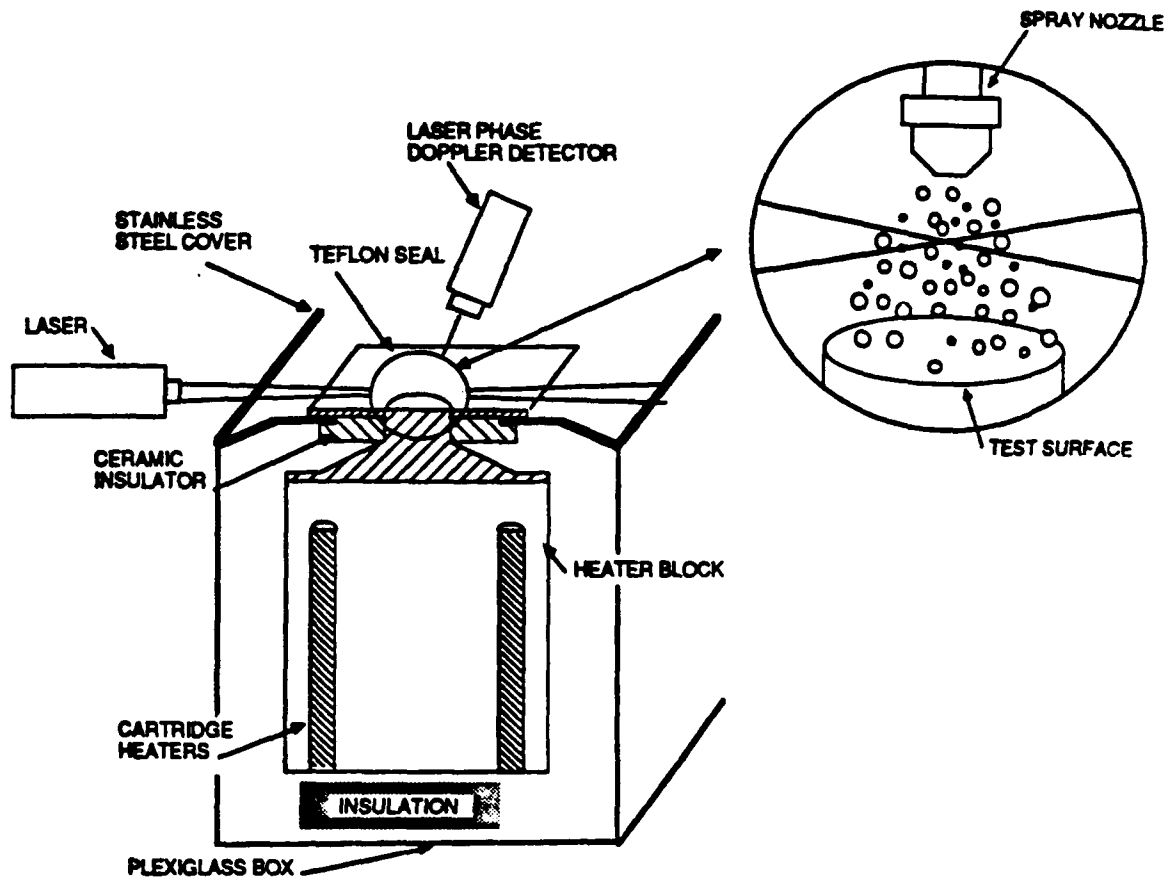
Figure 4.1.1: **Preliminary experimental apparatus**

For each experimental run, the following procedure was followed:

1. The surface was cleaned with acid to remove any oxidation or dirt.

2. The nozzle pressure was set to the desired value.

3. The power to the heater block was gradually increased at a rate slow enough to ensure quasi-steady measurements. The energy stored in the section just below the test surface was less than 0.1 percent of the heat removed by evaporation. This percentage was monitored and kept as low as possible for all runs.

4. When the critical heat flux was reached, or the heater block temperature became too high, the heater power was turned off and the experiment was terminated.

4.2 PRELIMINARY EXPERIMENTAL RESULTS

Figure 4.2.1 presents preliminary experimental results obtained by the method described above. Nozzles 1 through 4 were all operating at 20 psig. The nozzle characteristics at this pressure are presented in Table 5.1.1 in the analysis section of the report. These first experiments show that a heat flux of over 1,100 W/cm^2 is removed with a surface temperature of 160 ^0C. We observed that the maximum heat flux increased with increasing flow rate. Since the nozzles are pressure atomizing nozzles, the droplet diameters and velocities should not vary significantly for the different orifice sizes at the same pressure. The main difference is in flow rate. Since the percentage of the spray which is entrained or rebounded is dependant mainly on the droplet velocity and diameter distribution, the critical heat flux should be proportional to the flow rate. Examination of Figure 4.2.1 does substantiate this conclusion.
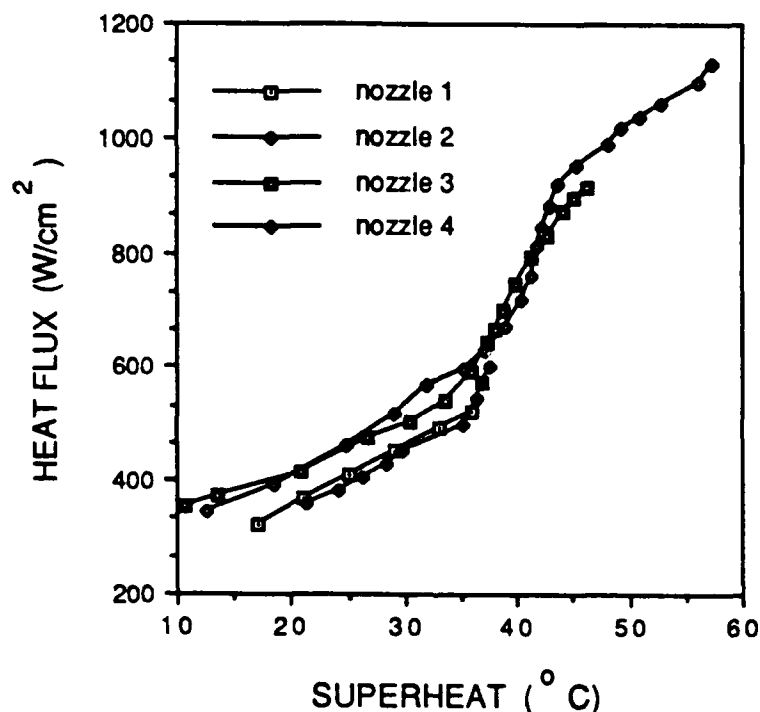
Figure 4.2.1: Preliminary experimental results

8

We observed during all the experiments that the critical heat flux was always preceded by a dryout in the center of the surface which propagated radially outwards as the heat flux was increased. We believe that this dryout was being caused by a deficiency in liquid supply at the center of the surface. Even though the overall flow rate was much higher than was required to remove the heat being supplied to the surface. This indicates that the spray conditions were not ideal, and a large percentage of the coolant was either being entrained or rebounded from the surface resulting in reduced heat removal capability. Since dryout always began in the center of the surface, we decided to perform an analysis of the spray characteristics directly above the center of the surface to determine the reason for the deficiency. This analysis and the conclusions are presented in the following section.

V. SPRAY CHARACTERISTICS ANALYSIS

As discussed in the previous section, the spray characteristics
directly above the center of the surface were measured using a laser
phase Doppler system and analyzed to determine the phenomena leading to
the CHF. The measurements include droplet velocity, droplet diameter,
and volume flux distributions for various experimental conditions. This
section describes these measurements, the data obtained, and the
relationships between the spray characteristics and the heat transfer
results. An in-depth analysis of the effects of the spray
characteristics on the heat transfer for one experimental case is
presented. The results of this analysis are then used to explain the
heat transfer results for the other preliminary experimental cases
presented in the previous section.

5.1 MEASUREMENT AND ANALYSIS

For the experimental results already presented, four different
spray nozzles were used. The characteristics of these nozzles,
operating at various pressures, govern the heat transfer. Knowledge of
the droplet diameter and velocity distributions, and the volume flux
profiles is of vital importance to the understanding and analysis of the
experimental results. Table 5.1.1 shows the orifice diameter, nominal
volumetric flow rate, and spray cone angle for the four nozzles tested.
More important information concerning the spray characteristics was
obtained using a laser phase Doppler system.

Table 5.1.1: Nozzle characteristics

Nozzle	Orifice dia. (in)	Flow Rate (1/hr) 20 psig	30 psig	40 psig	Cone Angle 20 psig	40 psig
1	0.020	9.5	11.8	13.6	50^0	58^0
2	0.022	13.0	12.9	15.7	56^0	60^0
3	0.027	19.3	22.7	27.3	54^0	59^0
4	0.030	22.7	27.3	31.8	54^0	60^0

The laser phase Doppler system used for this study was an
Aerometrics Phase Doppler Particle Analyzer (PDPA). A detailed
theoretical discussion of the procedure is reported in reference [16].
The optical configuration of the PDPA is the same as that of a
conventional laser Doppler velocimeter. Light is scattered from
transparent spherical droplets passing through the fringe patterns
formed by the intersection of two laser beams. This scattered light
produces another interference fringe pattern in the far field which is
imaged on an aperture. The spacing of the fringes in this pattern is
directly proportional to the droplet diameter. As the drop moves, the
fringe pattern is swept across the aperture. Its passing is observed by
three detectors located at selected spacings behind the aperture. The
signal produced by each of these detectors is identical in frequency
content which is used to determine the droplet velocity. However,
because of the spatial separation employed between the detectors, a
phase difference exists between the signals. This phase shift is
proportional to the fringe spacing and therefore the droplet diameter.

Measurements of the droplet velocity, diameter and volume flux
distributions were made under various experimental conditions. The
volume flux distribution for nozzle 2 operating at 20 psig was measured
for the cold spray with no surface present. The curve presented in
Figure 5.1.1 shows the volume flux distribution plotted against radial
position within the spray. All laser phase Doppler measurements were
taken at a distance of 1.55 cm from the nozzle exit (0.35 cm above the
test surface). The values presented in Figure 5.1.1 were adjusted
slightly such that the volume flux distribution integrated over the
surface area gives the actual volume flow rate leaving the nozzle. The
actual measured values were within three percent of the adjusted values
presented. When these measurements are repeated when the test surface
is present, the volume flux measurements cannot be used because they do
not distinguish between liquid coming to the surface and liquid leaving
the surface by rebound or entrainment.

Experimental observations indicate that the maximum heat flux
results from a deficiency in liquid supply to the center of the surface.
Transition to a film boiling condition begins with the formation of a
vapor barrier in the center of the surface which propagates radially

11

outward as the heat flux increases. Therefore, the onset of film boiling may be predicted through analysis of the spray conditions at the center of the surface. This may be accomplished by comparing the heat removal capability of the volume of coolant delivered to the surface to the heat flux at the center of the surface. When the heat delivered to the surface surpasses the heat removal capability of the spray, the deficiency in liquid supply results in surface dryout. As the surface becomes dry, the surface temperature increases rapidly to the point at which it becomes nonwetting. This is the onset of film boiling.
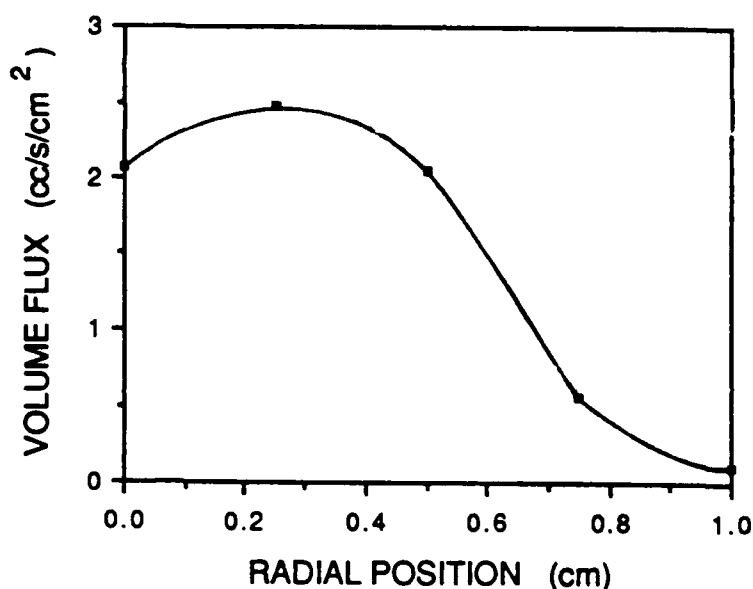
Figure 5.1.1: Volume flux distribution

The volume of coolant delivered to the surface can be calculated from the laser phase Doppler measurements in the following manner.

1.   Laser phase Doppler measurements of the droplet diameters and velocities at a distance of 3.5 mm above the test surface are obtained.

2.   The diameter measurements are then used to calculate the percentage of the volume of coolant supplied to the surface, which comes back off the surface by entrainment in the escaping vapor, rebound and splashing, or expulsion from

12

nucleating bubbles. The droplets with positive velocities are approaching the surface. Those with negative velocities are leaving.

3. This percentage is used in conjunction with volume flux at the center of the surface given in Figure 5.1.1 to determine the volume flux which is available for heat removal.

4. The total heat removal capability of this volume flux, both sensible and latent, is then compared to the actual heat flux to determine if a deficiency is present. The critical heat flux is predicted by this comparison.

The method described above is used to plot the curve given in Figure 5.1.2 for nozzle number 2 operating at 20 psig. The total heat removal capability of the spray is plotted against the heat flux. The intersection of this curve and the straight line indicates the point where the heat removal capability equals the heat flux to the center of the surface. As the curve drops below this line, the deficiency in liquid supply leads to the onset of film boiling. Therefore, the maximum heat flux should result at a slightly higher heat flux than indicated by the intersection. Figure 5.1.3 shows the corresponding heat flux versus ΔT curve. The critical heat flux occurs at 814 W/cm^2, which is only slightly higher than the heat flux at the intersection at approximately 780 W/cm^2 in Figure 5.1.2. This indicates that the CHF can indeed be predicted through an analysis of the spray characteristics.

Further analysis of Figure 5.1.2 indicates that the three regions labeled on the heat transfer curve in Figure 5.1.3 can also be explained. The division between region I and region II is defined by the point where the sensible heat removal capability is equated to the heat flux. At the lower heat fluxes in region I, heat is predominantly removed by raising the temperature of the coolant to the saturation temperature. Liquid in close proximity to the surface evaporates. A portion of this vapor recondenses delivering its latent heat to

subcooled liquid in the vicinity. This is similar to subcooled flow
boiling. Above this point, the percentage of heat removal attributed to
evaporation increases. After the majority of the coolant is at the
saturation temperature, a large increase in evaporation rate can occur
with little increase in surface temperature. This results in the
increasing slope (heat transfer coefficient) observed in Figure 5.1.3.
The division between regions II and III is seen where the slope of the
curve in Figure 5.1.3 begins to flatten. This corresponds to rapidly
decreasing heat removal capability as seen in Figure 5.1.2 due to
increased droplet entrainment, splashing, and expulsion. The
entrainment increases with heat flux because the vapor escape velocity
increases. The splashing increases because the liquid film surface
becomes more unstable due to increased nucleation. Expulsion also
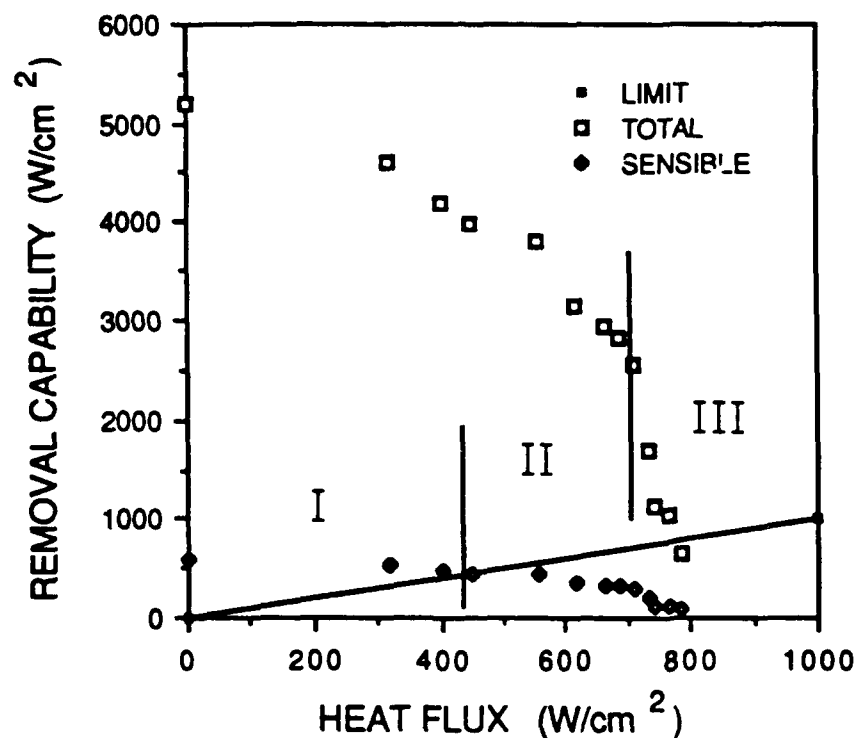increases due to increased nucleation and bubble generation frequency.

Figure 5.1.2: Heat removal capability

When the liquid supply becomes deficient, if the heat flux is
increased slightly, the energy cannot be removed. Therefore, it goes

14

into storage causing a large surface temperature increase. In this case, the surface temperature quickly exceeds the Leidenfrost temperature, and the surface becomes nonwetting (CHF is past).
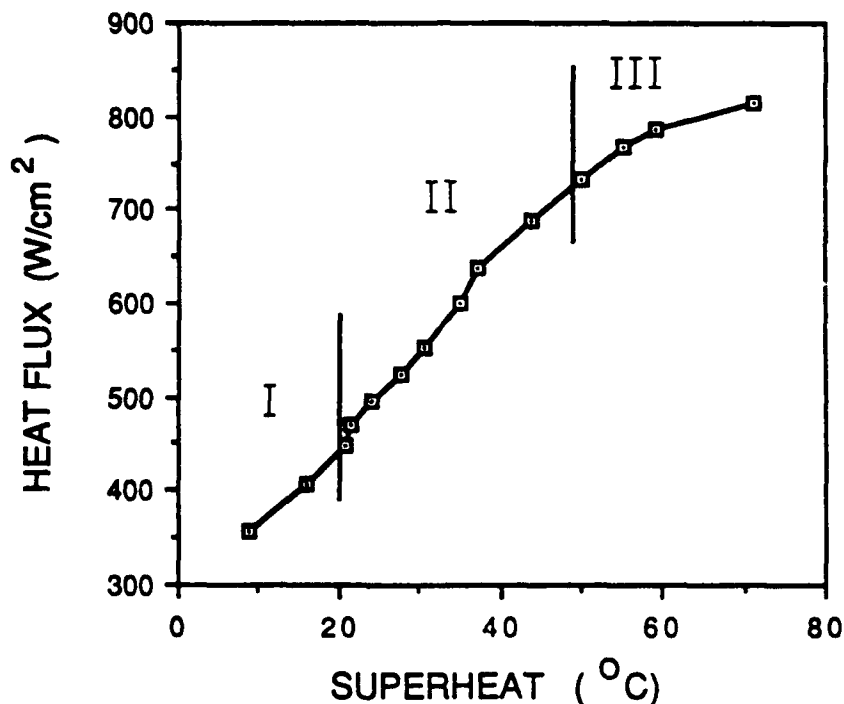

Figure 5.1.3: Heat flux vs. superheat, test case

As discussed in the previous section, the curves plotted in Figure 4.2.1 indicate that there are different heat transfer mechanisms which occur in the wetting region. For these cases, it appears that until the surface superheat reaches approximately 35 °C, the heat transfer is predominantly due to forced convection. This is evident due to the linear dependence of heat flux on the superheat. This is equivalent to region I shown in Figure 5.1.3 which indicates that the sensible heat of the liquid supply is sufficient to remove the entire heat flux. Above 35 °C, the liquid supply begins to deplete because of increased evaporation rates resulting in more efficient evaporation heat transfer (region II). This continues until the liquid supply becomes insufficient to sustain the heat flux. At this point, the surface temperature begins to rise rapidly until the critical heat flux is reached (region III). Some of the curves do not show this rise because

data points were taken at 5-minute intervals. When the liquid supply becomes deficient, the critical heat flux is reached very quickly. At the critical heat flux, roughly 20 percent of the fluid sprayed at the surface is evaporated. This is in agreement with the measurements of the percentage of liquid supplied which comes back off the surface, discussed in the previous section. This percentage is relatively constant for different nozzles operating at the same pressure. This is because the droplet velocity and diameter distributions are similar for each of the nozzles. The only significant difference in the nozzles is the volume flux of coolant. Therefore the maximum heat flux should be directly proportional to the volume flux for all the cases in Figure 4.2.1 which is the case as previously mentioned.

To identify the most ideal spray conditions, we need to determine the proper droplet size and velocity such that rebound and entrainment are avoided. Since the droplet diameters and velocities are measured a distance of 3.5 mm above the surface, this information can be determined by balancing the inertia of the droplet and the drag on the droplet using the following equation.

$$(u-v) = (u-v_o)\exp(-18\mu t/\rho d^2) \tag{5.1.1}$$

The above equation is numerically integrated for a given heat flux between the measurement probe area and the test surface to determine whether or not a given droplet is entrained in the escaping vapor. If not, the impact velocity is used to calculate the impact Weber number by the following equation.

$$We = \frac{\rho d v^2}{\sigma} \tag{5.1.2}$$

At Weber numbers greater than 80, droplet disintegration and rebound usually occurs for dry surfaces [17]. However, no information is available on rebound and splashing when the surface is covered a thin liquid film. The liquid film can deform and and absorb some of the kinetic energy of the impinging droplets. Equations 5.1.1 and 5.1.2 indicate that with large diameter and velocity droplets, entrainment is

less likely while rebound and splashing is more likely. Therefore, to minimize excess coolant requirements, the droplet diameters and velocities should fall within a certain range. If the diameters and velocities are too low, the droplets will be entrained in the escaping vapor, thus limiting the critical heat flux. If the diameters and velocities are too large, the droplets will cause rebound and splashing.

Figure 5.1.4 is a plot of a theoretical ideal droplet diameter and velocity range, which will minimize entrainment and rebound, at a heat flux of 766 W/cm^2. For this calculation it was assumed that droplets with impact Weber numbers greater than 80 caused rebound and splashing. The droplets with diameters and velocities below the entrainment curve will not reach the surface. Those with diameters and velocities above the rebound curve will disintegrate and rebound assuming the surface is predominantly dry. Curves such as this can be plotted for any desired heat removal rate. These curves can be very useful for low heat flux applications in which no excess coolant is present. In this type of spray cooling, the surface is not flooded but covered with isolated wet patches. This type of spray cooling is modeled and discussed in section 5.2 and demonstrates good comparison with experimental results.
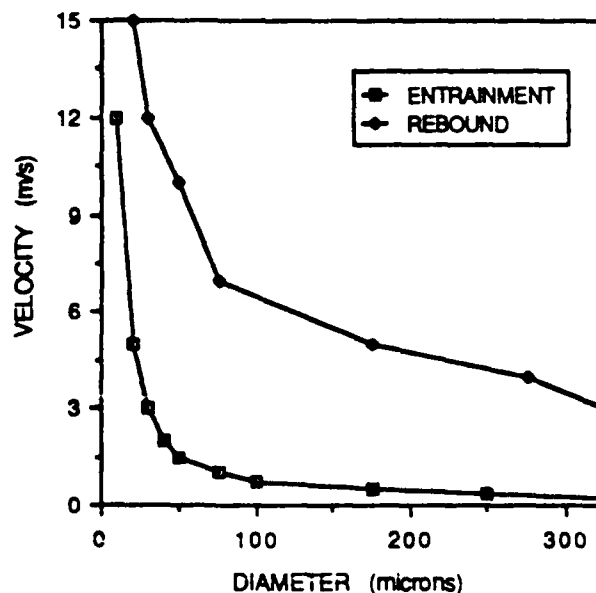

Figure 5.1.4: Ideal droplet diameter and velocity range

5.2 THEORETICAL MODELING

The preliminary research has indicated that the spray
characteristics greatly influence the heat transfer process. We believe
that droplet diameters and velocities can be supplied in an ideal range
such that no entrainment or rebound will occur. If this is done, the
next step is to determine which droplet diameters and velocities within
the range provide the most efficient heat transfer.

A preliminary analytical model to predict the most efficient heat
transfer conditions is presented in this section. The model is based on
the solution of the transient conduction problem from a heated solid
surface to an evaporating droplet. The model is based on a problem
definition similar to that presented by Rizza [18]. Rizza's model
allows for the possibility of surface flooding. However, his results
are not presented in a fashion which is easy to use. His model also
required the assumption that the thermal capacity of the surface was
negligible. He therefore solved the steady-state problem at each time
step based on the time dependant droplet geometry.

The previous data analysis suggested that for every heat flux,
there exists an ideal droplet diameter and velocity range such that none
of the impinging liquid will be entrained in the escaping vapor, or be
rebounded from the surface. The goal of this model is to identify the
most efficient droplet diameters, velocities and liquid distributions on
the surface that fall within the ideal range for a given heat flux. It
is hypothesized that smaller droplets and higher degrees of surface
saturation will provide the lowest surface temperature for a given heat
flux. The reason smaller droplets are thought to be more efficient is
because they maximize the perimeter to volume ratio and form thinner
liquid films on the surface. The perimeter to volume ratio is important
because at the perimeter, the liquid/vapor interface contacts the
surface allowing evaporation to occur with essentially no superheat.
The thinner liquid films are also more efficient because heat may be
conducted through the film for evaporation at the upper liquid/vapor
interface. Also, any nucleating bubble quickly breaks through the film
resulting in more liquid/vapor interface contacting the solid surface.

18

5.2.1. Model Approach

The approach to the solution of the model is as follows:

1. First a heat flux is chosen and the ideal droplet diameter and velocity range is calculated as discussed previously in the report.

2. Next, a droplet diameter and surface saturation from the determined range is chosen.

3. The required liquid mass flow rate necessary to remove the heat flux with no excess liquid is then calculated. Also, the ratio of initial droplet radius to the radius of one unit cell based on the selected droplet diameter and surface saturation is calculated.

4. The transient conduction problem for the heat conducted through the solid to the evaporating drop is solved using the governing equations and solution scheme which follow.

5. The surface temperature is integrated over time and area to output a value for a q vs. ΔT plot.

6. The procedure is repeated for different droplet diameters over the entire range for a variety of different surface saturations, This will give differing values of ΔT for each heat flux depending on the spray conditions.

7. A new heat flux is chosen and the entire process is repeated to yield heat flux versus superheat curves which show the effects resulting from changes in the spray conditions.

5.2.2. Governing Equations

The governing equations and the boundary conditions as they apply to the problem depicted in Figure 5.2.1 are presented here. Figure 5.2.1 is representative of one unit cell of the surface containing one

evaporating droplet (not shown). This model is only good for surface
saturation levels low enough that droplet conglomeration does not occur.
The conduction problem is only solved in the solid. This is due to the
complex nature of the heat transfer within the droplet. If conduction
alone is assumed to occur in the droplet artificially high temperatures
occur. In reality, bubble nucleation would occur with only slight
surface superheats. Any nucleating bubble would very quickly break
through the liquid surface resulting in the very efficient "perimeter"
type heat transfer previously discussed. For this reason, the model
assumes the surface to remain at the saturation temperature under the
evaporating droplet ($0 \leq r \leq r_d(t)$, $x = l$) This assumption may result
in underprediction of the surface temperature by as much as 20 ^{0}C.
However, the prediction of the general trend of the behavior is most
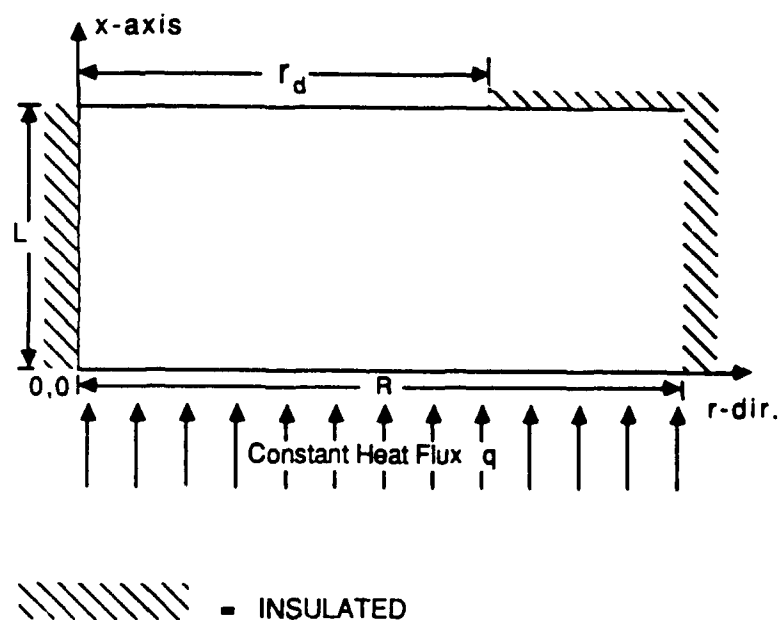likely accurate.

Figure 5.2.1: **Model geometry**

The transient conduction equation is

$$\frac{\partial^2 T}{\partial r^2} + \frac{1}{r} \frac{\partial T}{\partial r} + \frac{\partial^2 T}{\partial x^2} = \frac{1}{a} \frac{\partial T}{\partial t} \qquad (5.2.1)$$

The boundary conditions are

1.
$$\frac{\partial T}{\partial r} = 0, \text{ at } r = 0$$

2.
$$\frac{\partial T}{\partial r} = 0, \text{ at } r = R$$

3.
$$-k_s\frac{\partial T}{\partial x} = q, \text{ at } x = 0$$

4a.
$$T = T_{sat}, \text{ at } x = l, \ r \leq r_d(t)$$

4b.
$$\frac{\partial T}{\partial x} = 0, \text{ at } x = l, \ r > r_d(t)$$

The droplet radius is determined as a function of time by integrating the heat flux at the surface under the droplet and equating it the the evaporation rate.

$$\frac{\partial m}{\partial t} h_{fg} = - 2\pi \int_0^{r_d} k_s \frac{\partial T}{\partial x}\bigg|_{x=l} r dr \qquad (5.2.2)$$

The evaporation rate is then used to determine the decrease in droplet volume. The new radius is determined by assuming the the droplet shape remains constant as the volume decreases.

The governing equation and boundary conditions are then nondimensionalized using

$$\eta = r/R, \quad \lambda = x/l, \quad \tau = t/t_{res}, \quad \text{and} \quad \theta = (T-t_{sat})/T_{sat}$$
$$\delta = d/R, \quad V = V/R^3, \quad \phi = \frac{ql}{k_s T_{sat}}$$

The resulting dimensionless equation and boundary conditions are given by

$$\frac{\partial^2\theta}{\partial\eta^2} + \frac{1}{\eta}\frac{\partial\theta}{\partial\eta} + \left[\frac{R}{l}\right]^2\frac{\partial^2\theta}{\partial\lambda^2} = \frac{1}{Fo}\frac{\partial\theta}{\partial\tau} \qquad (5.2.3)$$

21

1. $\qquad \dfrac{\partial \theta}{\partial \eta} = 0$, at $\eta = 0$

2. $\qquad \dfrac{\partial \theta}{\partial \eta} = 0$, at $\eta = 1$

3. $\qquad \dfrac{\partial \theta}{\partial \lambda} = \phi$, at $\lambda = 0$

4a. $\qquad \theta = 0$, at $\lambda = 1$, $\eta \leq \eta_d(\tau)$

4b. $\qquad \dfrac{\partial \theta}{\partial \lambda} = 0$, at $\lambda = 1$, $\eta > \eta_d(\tau)$

$$\frac{\partial V}{\partial \tau} = - (\pi/3)\phi \delta^3 \int_0^{\eta_d} \left.\frac{\partial \theta}{\partial \lambda}\right|_{\lambda=1} \eta d\eta \qquad (5.2.4)$$

5.2.3 Solution Scheme

The governing equations are solved using the Alternating Direction Implicit solution scheme. The equations are first written in finite difference form using forward or central differencing. They are written for the first half time step in the λ-direction (All terms in λ-direction written as unknowns). These equations result in a tridiagonal matrix which is easily solved using the Thomas Algorithm [19]. These new temperatures are then used in the equations written in the η-direction for the second half time step resulting in another tridiagonal matrix. This matrix is then solved to give the new temperature distribution. The heat flux at the surface is then integrated to decrement the droplet radius. The temperatures are then updated and the solution continues. When the drop completely evaporates, a new drop is added and the problem is solved again using the temperature profile at the end of the previous droplet as the initial temperature profile for the new droplet. This continues until the temperature profiles no longer change from one droplet to the next. At this point the surface temperature is integrated over the total area and the lifetime of the droplet to provide the average surface temperature estimate.

22

5.2.4 Model Results

The computer program has been written and some results presented in this section. The output includes a prediction for the surface temperature averaged over the surface area and the lifetime of the droplet for various values of heat flux, surface saturation, and droplet diameter before impact. The results verify the anticipated trends of improved efficiency with increasing surface saturation and decreasing droplet diameter. Figures 5.2.2 and 5.2.3 are plots of heat flux versus surface superheat for varying values of surface saturation and droplet diameter, respectively. These curves illustrate the extreme importance of the spray characteristics and the liquid distribution on the surface. The results clearly indicate that any changes in surface saturation or droplet diameter have extreme effects on the resulting surface superheat for any given heat flux. The predictions presented do not include the account for any heat transfer resistance within the liquid. Since this resistance can dominate, the predictions are only useful in showing the anticipated trends. We should also mention that the predictions are the ideal maximum. Any nonuniformity in the liquid distribution could result in a much higher average surface temperature. The same holds true for any variation in droplet diameter.

Since the model underpredicts the surface superheat because of the assumption that the surface remains at the saturation temperature under the evaporating droplet, a conduction drop is added for comparison with experiments. The correction uses a time and area averaged resistance, R_h, to estimate the conduction drop in the droplet. Equations 5.2.5 and 5.2.6, from reference 3, calculate the temperature drop which is added to the superheat given by the model predictions.

$$R_h = \frac{4/9}{\pi d\beta^2 k_l} \qquad (5.2.5)$$

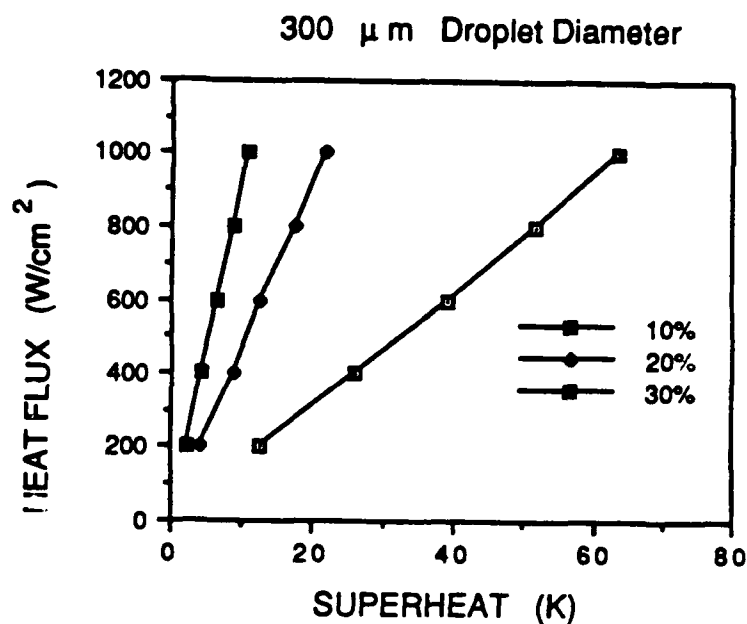$$\Delta T = \pi R^2 q / R_h \qquad (5.2.6)$$

300 μm Droplet Diameter

Figure 5.2.2: **Effects of surface saturation**
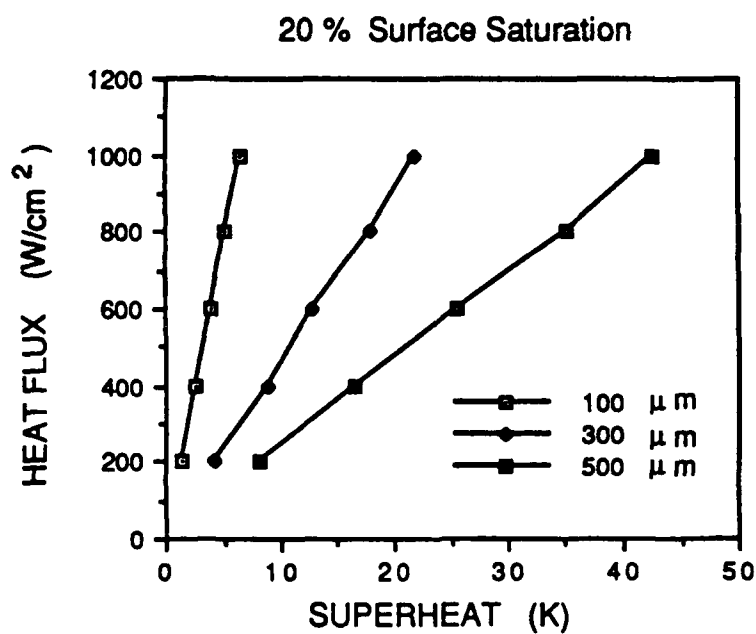
20 % Surface Saturation

Figure 5.2.3: **Effects of droplet diameter**

5.2.5 Comparison With Other Experimental Results

The analytical model predictions are compared to the experimental results presented by Bonacina et al. [3]. We feel these results are most applicable because no excess liquid was present and the average surface saturation values were low. In general, the model predictions are well supported by the experimental data. Table 5.2.1 shows a comparison of the model and the experimental results. The value of ΔT_{exp} was taken from the data presented by Bonacina et al. The ΔT_{thr} is predicted by the analytical model, including the conduction drop across the liquid film, estimated as described above. The percent difference between the theoretical and experimental results is also given.

Table 5.2.1: Comparison with experimental data

Run	q	ϵ	d	ΔT_{exp}	ΔT_{thr}	% Diff
	W/cm^2		μm	K	K	
1	49.7	0.045	65	18.0	16.1	10.6
2	64.8	0.188	56	4.5	4.0	9.1
3	109.9	0.195	83	11.9	11.9	17.6
4	142.0	0.054	73	39.4	42.7	8.4
5	215.3	0.196	90	23.9	20.8	13.0

The agreement between the model and the experimental data of Bonacina et al. is very good. In most cases, the surface temperature is underpredicted by the model. This is probably due to variation in the droplet diameter and nonuniformity in the liquid distribution on the surface.

5.3 DISCUSSION

From the results of the preliminary experiments and the analytical model, apparently several factors influence the heat transfer efficiency. These include the wetting characteristics of the surface, the percent of surface saturation, the thickness of the wet patches, and the wet patch perimeter to volume ratio.

Wetting Characteristics: The wetting characteristics influence the heat

transfer efficiency because the contact angle influences the thickness of the wet patches. To maximize the efficiency, the contact angle should approach zero degrees.

Surface Saturation: The heat transfer efficiency is highly dependent on the surface saturation. This is because the dry areas remove a negligible amount of heat in comparison to the wet areas. Therefore, if the surface is only 10 percent wet, the heat flux to the wet patches is 10 times greater than the average heat flux to the entire surface. As the heat flux to a given wet patch increases, the surface temperature must also increase. Therefore, higher surface saturation provides more efficient heat transfer if all other factors remain constant. However, the surface saturation should not be increased to the point where wet patches begin to conglomerate because this will adversely affect the wet patch thickness and perimeter to volume ratio. The data of Bonacina et al. substantiate this observation. For the same heat flux and droplet diameter, a 47 percent increase in surface saturation yielded a 58 percent increase in heat transfer coefficient [3].

Wet Patch Thickness: The wet patch thickness influences the efficiency because evaporation occurs at the upper liquid vapor interface. Therefore, the heat must be conducted through the liquid film. Thicker films will result in higher temperature differences across the film. Since the liquid vapor interface is at the saturation temperature, the surface temperature must increase with liquid film thickness.

Wet Patch Perimeter To Volume Ratio: The wet patch perimeter to volume ratio has a very strong influence on the heat transfer coefficient. This is because intense evaporation occurs at the perimeter of the droplet where the liquid/vapor interface contacts the surface. Also, very little temperature drop is required to sustain evaporation at the perimeter. For a given volume of liquid on the surface, smaller droplets would provide more perimeter area, thus improving the heat transfer efficiency. This conclusion is also substantiated by the data of Bonacina et al. They also show an increase in heat transfer coefficient with a decrease in droplet diameter [3].

26

VI. IMPROVED EXPERIMENTATION

The preliminary experiments and analysis gave much insight into understanding the spray cooling process. In the preliminary experiments, near the critical heat flux, only 20 percent of the coolant supplied resulted in effective heat removal. Since the spray characteristics were such that a large portion of the supply was rebounded, we decided to use nozzles supplying smaller, lower velocity droplets. Also, we discovered certain problems with the initial apparatus; mainly, because of the high thermal mass, accurate determination of the critical heat flux was difficult. For very high heat fluxes, the temperature of the heater block approached the melting point of copper. We decided that a new apparatus would be designed using finite element analysis to minimize the thermal mass and the maximum temperature in the heater block. The new apparatus would also feature power control based on temperature rather than heat flux. This section describes the new apparatus, its benefits, and new experimental results. These results are also analyzed based on the findings previously presented in this report.

6.1 EXPERIMENTAL DESCRIPTION

Owing to the large thermal gradients required to drive large heat fluxes through any surface, we must carefully design the apparatus so as to arrive at temperatures within the body which maintain the physical and chemical integrity of the system. A number of methods of heating a surface have been considered, namely:

(1) Induction heating: If a material which is electrically conductive is subjected to a strong, high frequency magnetic field, then large eddy currents are set up within, which dissipate energy due to the electrical resistance of the material. Second, if the material is magnetic, then losses due to hysteresis also contribute to the heat generation. Coupled with this are also mechanical losses due to magneto-constriction of the material. This technique, however, requires the electromagnetic coils to be as close as possible to the surface, thereby, restricting access to the droplet sprays. Also the high frequency magnetic field

induces currents in the thermocouples circuits, making temperature measurement and control difficult.

(2) Resistive heating: In this case, the surface consists primarily of a resistor film of good thermal and electrical properties. Electric current flowing against the resistance generates heat which is conducted away from the surface by the droplets. The heat flux is given by the product of the voltage across the heater times the current flowing through it. Current material properties require very thin films which are easily destroyed when the surface temperature jumps past the Leidenfrost temperature. Thus regular fabrication and replacement of the surface is needed.

(3) Radiation heating: The surface is heated using incident thermal radiation from high power tungsten-in-quartz lamps. Using specially contoured air cooled or refractory reflectors the incident flux can be tailored to be uniform on the surface.

The above three methods provide:

    (a) Quick transient response in terms of switching the power or heat flux on and off immediately,

    (b) Heat flux is uniform over the surface,

    (c) Surface has a lower thermal capacity giving better transient control of average surface temperature,

    (d) High heat flux rates ($1,500$ W/cm^2) are feasible if the system can be maintained at a temperature much lower than the melting or oxidation points of the material.

The radiative method of heating is the most appropriate for the scale of experiments projected in this study. With reference to Figure 6.1.1, higher power (40 W/cm) tungsten-in-quartz heat lamps are inserted into cylindrical chambers within the copper body of the heated surface. This system, i.e., the tungsten filament, which can be viewed as a line element radiative heat source, (temperature $= 4,000$ ^0F, $0.5 \leq \lambda \leq 4.5$ μm), enclosed within a cylinder closed at its ends, constitutes a black body. Thus, all the radiative energy is absorbed into the copper base of the heated surface. These radiation lamps have a fast thermal response (99 percent rated power within 3 secs), can withstand high temperatures by virtue of their sealed quartz envelope, and provide a

high radiative heat flux. Depending on the heat flux required, a
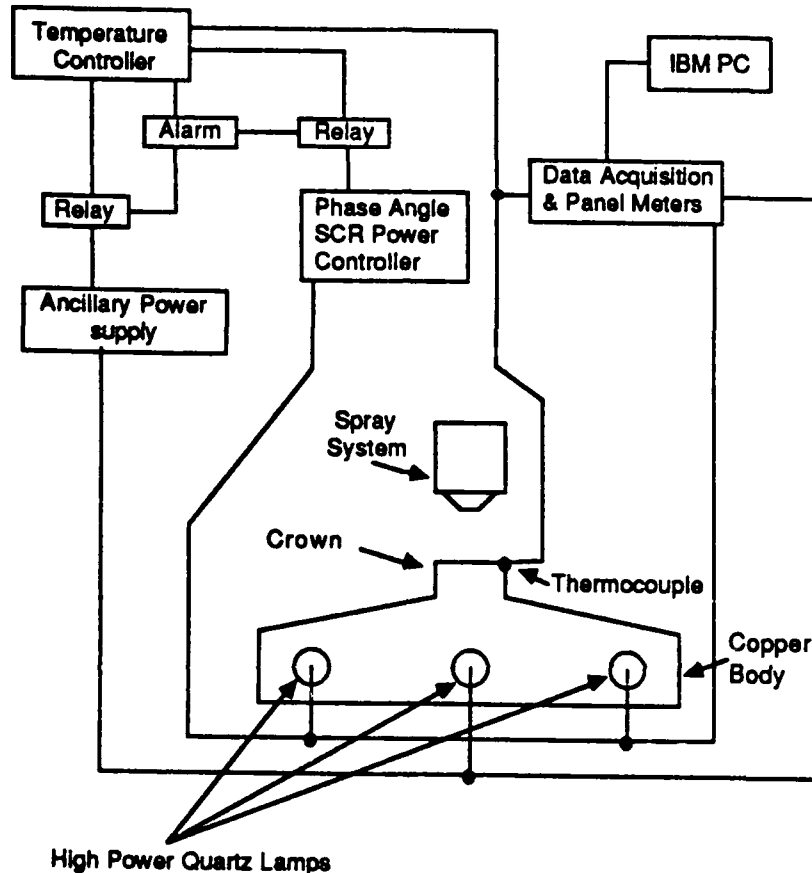multiple number of these lamps can be used in this setup.

The temperature controller, as shown in Figure 6.1.1, monitors the
temperature of the thermocouple surface, maintaining it at some preset
value by sending a control signal to the Phase-Angle SCR power supply,
which in turn regulates the power to the quartz lamps by varying the
phase angle on each ac cycle proportional to the control signal. A
second ancillary variable transformer power supply acts as a backup for
peak loads. If the temperature of the surface overshoots, an alarm
disconnects the power to the heaters via relays. The power to the lamps
along with the temperatures are continuously indicated by the panel
meters and recorded by the data acquisition system. All process
parameters are displayed and stored on the PC. The temperature

controller which is programmable, uses a PID, (proportional, integral and derivative) scheme, performing a maximum of six cycles a second and maintains the temperature within 1 ^{0}C of set point.

6.1.1 Temperature and Heat Flux Determination

The heat source consists of two parts, (Figure 6.1.2), namely, the lower copper body into which are inserted the radiation lamps, and the crown or cooled surface from which heat removal is desired. By measuring the temperature difference across a known distance in a section of the crown where the isotherms have flat profiles, we can determine the heat flux using Fourier's law of heat conduction,

$$q = -K\frac{\Delta T}{\Delta x}$$ (6.1.1)

At a desired heat flux of 1,000 W/cm^2, in a cop. r body of uniform cross section, the temperature gradient using equation (6.1.1) is

$$\frac{dT}{dx} = 25.4 \text{ oC/mm}$$ (6.1.2)

This requires that the size of the thermocouple be of the order of 40 μm for a temperature measurement resolution to be within 1 ^{0}C. Second, an uncertainty analysis

$$\frac{w_q}{q} = \sqrt{\left\{\frac{w_x}{\Delta x}\right\}^2 + \left\{\frac{w_T}{\Delta T}\right\}^2}$$ (6.1.3)

implies that the prediction of the heat flux is also dependent on the accurate measurement of the distance between the two thermocouples. Ideally, this parameter in the heat flux equation should be minimized for maximum temperature reduction within the system.
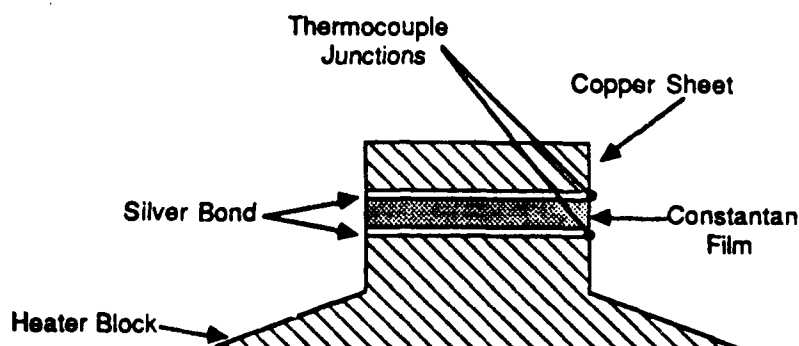
Figure 6.1.2:   Integral surface thermocouple junctions

We do not recommend the common method of temperature measurement
using fine thermocouples because as mentioned earlier, the wire sizes
required are too fine at such high temperatures, being more susceptible
to standard wire errors [20], corrosion and failure.

An alternative method to measure temperature is to use a thin film
of Constantan, (selected because with copper it composes a
thermocouple), interleaved between a copper film on the top, (which
constitutes the cooled surface), and the heated copper block at the
bottom, located in a region of the crown where flat isotherms are
predicted.

This laminate thermocouple construction, shown in Figure 6.1.2a, is
bonded together using silver solder, (Harris 50-003-1/4, 50% Ag + 15.5%
Cu + 16.5% Zn + 18% Cd, liquidus 1175 ^{0}F), selected because of the high
temperatures expected within the copper block. Constantan has a low
thermal conductivity, (21.12 W/m ^{0}K), thus the thinner the film, the
lower the temperature rise across it. Second, the film thickness
measurement, Δx, when accurately determined, further reduces the
uncertainty in the heat flux prediction.

Owing to the existence of a heat flux across the laminate
thermocouple junction, (see Figure 6.1.2a), and to the finite thickness
of the silver solder layer, (50-75 μm), we cannot assume the junction to
be isothermal as a temperature gradient exists. Hence, a simple
copper-constantan thermocouple calibration is invalidated. However, a
closer study reveals that the laminate can be viewed as two
thermocouples, namely, copper-silver and silver-constantan. Here, the

31
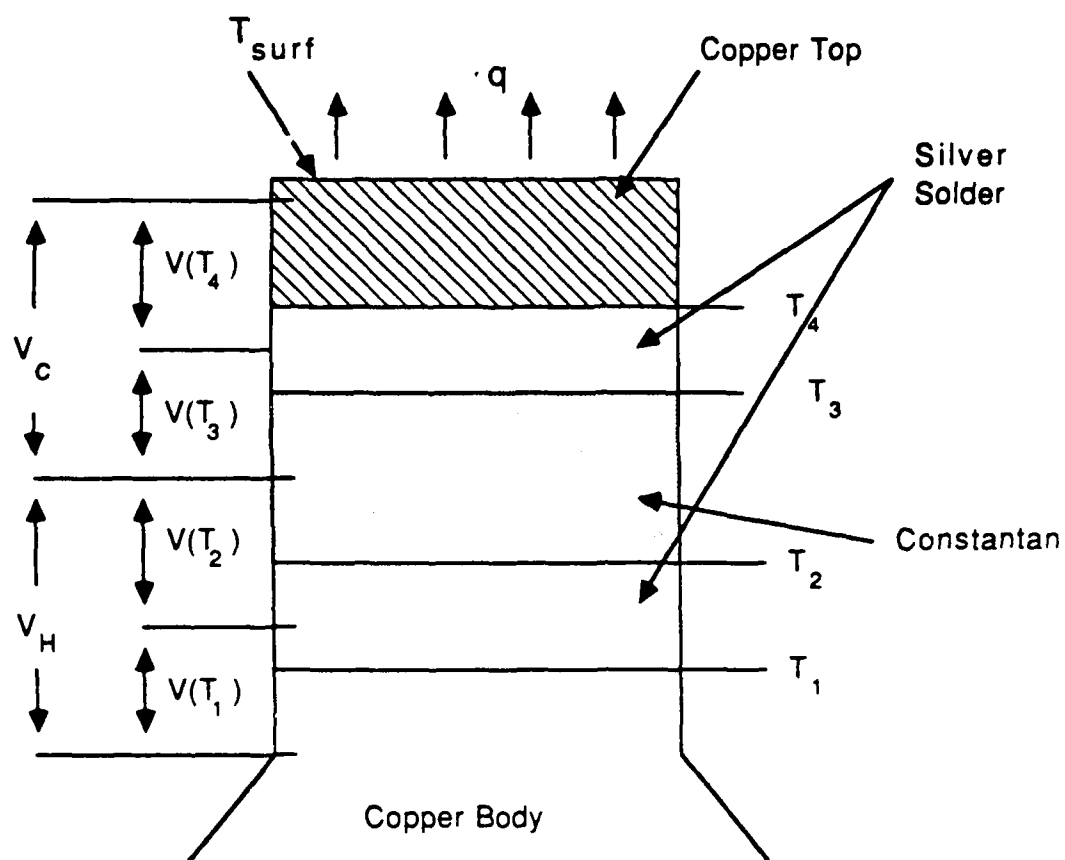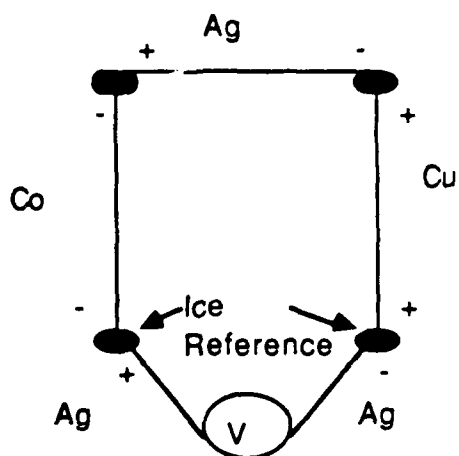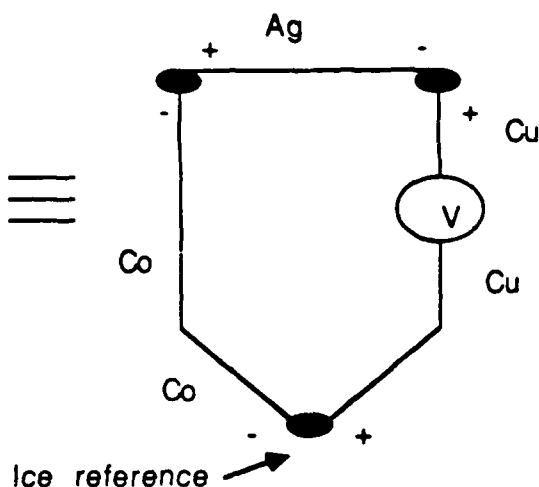
Figure 6.1.3: Thermocouple analysis

junctions are well defined planes marked by the boundaries of the constantan and copper. The resulting voltage measurements is the sum of the two thermocouples in series as shown in Figure 6.1.2b, the equivalent compensated circuit is shown in Figure 6.1.2c. This requires individual calibrations for both the copper-silver and silver-constantan thermocouples which were performed and the results are presented in Figure 6.1.3, along with their polynomial fits, provided in Table 6.1.1.

Table 6.1.1: Thermocouple calibration

Polynomial Coefficient	Copper-Cons antan CuCo	Copper-Silver CuAg	Constantan-Silver CoAg
a_0	7.2633364e-07	-8.2093389e-06	-5.3587533e-06
a_1	3.8522987e-05	1.5605573e-06	4.0999952e-05
a_2	4.3124505e-08	-1.0782581e-08	-5.3762608e-08
a_3	2.2868553e-11	1.8549296e-10	9.1690699e-10
a_4	-4.4466612e-13	-1.4160927e-12	-4.7932901e-12
a_5	1.7744421e-15	5.7250733e-15	1.4669923e-14
a_6	-3.3649500e-18	-1.1647572e-17	-2.5512934e-17
a_7	2.4993808e-21	9.3373451e-21	1.8473597e-20

Where, $V = a_0 + a_1 T + a_2 T^2 + \cdots + a_n T^n$ and

T = Temperature in degrees Celsius
V = Thermocouple voltage in volts

The corrected heat flux from the surface can then be written as

$$q = K_{Ag} \frac{T_1 - T_2}{\Delta x_{Ag}} = K_{Co} \frac{T_2 - T_3}{\Delta x_{Co}} = K_{Ag} \frac{T_3 - T_4}{\Delta x_{Ag}} \qquad (6.1.4)$$

from the first equality in (6.1.4) we get

$$\frac{K_{Ag}}{\Delta x_{Ag}} T_1 - \left\{ \frac{K_{Ag}}{\Delta x_{Ag}} + \frac{K_{Co}}{\Delta x_{Co}} \right\} T_2 + \frac{K_{Co}}{\Delta x_{Co}} T_3 = 0 \qquad (6.1.5)$$

Similarly from the second equality in (6.1.4) we get

$$T_1 - T_2 - T_3 + T_4 = 0 \qquad (6.1.6)$$

The voltages measured by the equipment are,

$$V(T_1) + V(T_2) = V_H \qquad (6.1.7)$$

$$V(T_3) + V(T_4) = V_c \qquad (6.1.8$$

We have four equations, 6.1.4 through 6.1.8 and four unknowns $T_{1,2,3,4}$. Having already obtained the calibrations for the various thermocouples, using a Gauss-Seidel iterative method. we can evaluate the unknowns.
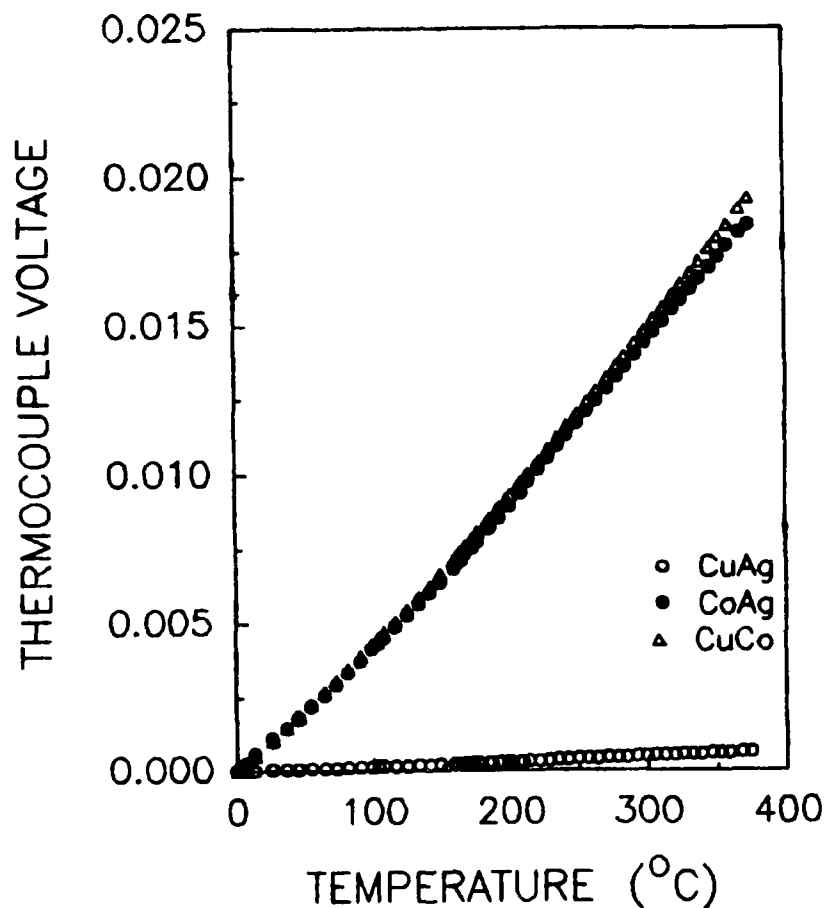

Figure 6.1.4: Thermocouple voltage calibration

The heat flux at the surface is given by equation (6.1.4) and the surface temperature is evaluated by extrapolation using equation 6.1.9,

$$T_{surf} = T_4 - q \frac{\Delta x_{Cu}}{K_{Cu}} \qquad (6.1.9)$$

Before fabrication of the heated surface, steady-state heat conduction analysis using finite element techniques were performed on the prototype. The lighted length of the lamps being 12.5 cm and the use of three lamps require the plan section of the body to be 12.5 cm by 7.5 cm. In the design of the heated surface body, we attempt to minimize the maximum temperatures and reduce the thermal mass. The lower temperatures not only preserve the physical and chemical integrity of the body, but in conjunction with the lower thermal mass provide quicker heating/cooling transients. Figure 6.1.4 provides results of this feasibility analysis. This is a symmetrical quarter section of the model, so sectioned to improve resolution and designed with a square crown of 1-cm edge and 7-mm height for simplicity of analysis. Two constantan films of 127-μm thickness are located 4 mm and 6 mm above the body surface. At locations above 3 mm, flat isotherms are observed. These results obtained for conditions of surface temperature of 150 ^{0}C and heat flux of 1,000 W/cm^2, indicate a maximum temperature of 567 ^{0}C at the lower most corner of the block. Experiments performed with a shortened crown of height 4.06 mm and a single constantan film, gave temperatures which corroborate well with the numerical predictions.
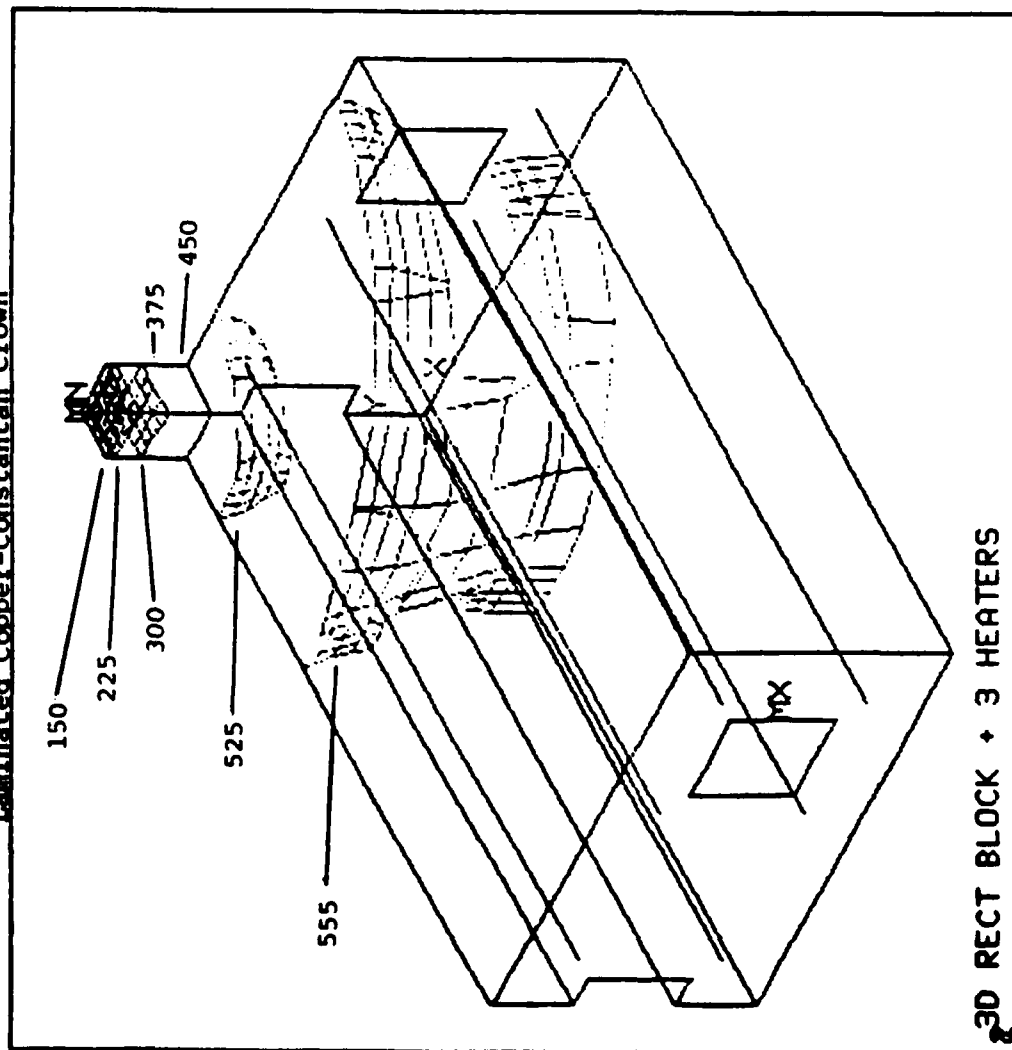
Figure 6.1.5: Finite element analysis of heater block

6.2 SPRAY SYSTEM

The components of the spray system are illustrated in Figure 6.2.1. City water is first distilled in a Barnstead distiller before being passed through a Barnstead Nanopure de-ionizer. Using a variable flow pump, the cold water is filtered before flowing through a calibrated orifice plate flow meter, designed for flow rates of 0.2 cc/sec and more. Because gas bubbles appear in the water lines, a gas trap is included which is integrated with a temperature controlled heater to provide water for the spray nozzle at some predefined temperature value. This facilitates control on the degree of subcooling. Finally, Paasche Air brushes are used as the spray nozzles. These nozzles are capable of providing homogeneous droplet sprays over small areas (approximately 15 mm diameter). A thin annular liquid stream is aspirated or injected into the path of an accelerating jet of air. Through surface shear forces, the air jet atomizes the liquid into small droplets (ranging in size from 40 μm to 220 μm depending on liquid and air flow rates) and imparts momentum to them. As the velocity of the air jet is increased, for the same liquid flow rate, the average size of the droplets decrease. Likewise, for the same air flow rate, as the liquid flow rate is increased, the size of the droplets increase; see results in Table 6.2.1, which presents velocity, droplet size and flow rates. The droplet diameter and velocity measurements are described in section 6.2.1.

A study of the air/droplet impingement flow field on the surface clearly shows the advantages of such a system. The air jet on impinging the surface forms the well studied stagnation point flow field [21]. The drops do not follow the air streamlines close to the surface but due to their relatively higher inertia follow straight paths, impinging on the hot surface to form flat discs, whose thickness is much smaller than the diameter of the drop. Simultaneously, the stagnation flow field spreads the droplet/discs further, like a rolling pin, to form a thin film on the surface. Any vapor that emanates from the hot surface because of evaporation is instantly swept away. A review of phase change thermodynamics will show that a liquid is induced to evaporate if the partial vapor pressure of its vapor in the ambient adjacent to its

surface is lower than the saturation vapor pressure at that temperature. Hence, the effect of the stagnation flow field is to enhance evaporation even further by clearing away/reducing the partial vapor pressure in the immediate vicinity of the liquid surface.
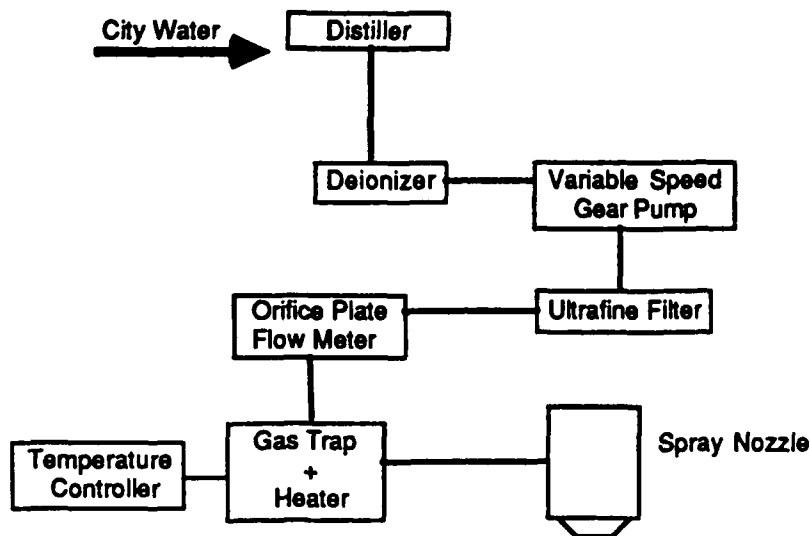

Figure 6.2.1: Spray system

6.2.1 Droplet Size and Velocity Measurement

The heat transfer depends on the surface conditions, surface temperature, properties of the liquid, droplet size and velocity. To define the thermal and fluid flow fields, we have experimented under controlled conditions within experimental limitations.

If a drop of water is brought to rest on the surface of a liquid with which it is completely immiscible, then surface tension analysis predicts that the angle at the junction where the two surfaces meet is fixed for the two liquids. Using this principle, a slide covered with a thin film of petroleum jelly is passed under the spray nozzle, where the droplets have lost most of their momentum (to prevent any splashing or breaking). The droplets then sit on the surface of the slide as schematically shown in Figure 6.2.2. These truncated spheres, (studies in droplet clouds have shown that droplets of diameter less than 3,000 μm maintain a spherical geometry, beyond this gravitational forces begin to skew the profile), have an apparent diameter, D, when viewed normal

38

to the surface of the plate, which is related to the actual diameter, d, through

$$d = D \left[\frac{2 + 3\cos\phi - \cos^3\phi}{4} \right]^{1/3} \tag{6.2.1}$$

Here, ϕ is the angle of contact between the two surfaces of the liquids, ($\phi \simeq 104^0$ for water and petroleum jelly). Using this method average droplet size and distributions were obtained for a fixed set of air and water flow rates. This method provides estimat   of droplets diameters that are accurate to within 10 percent.
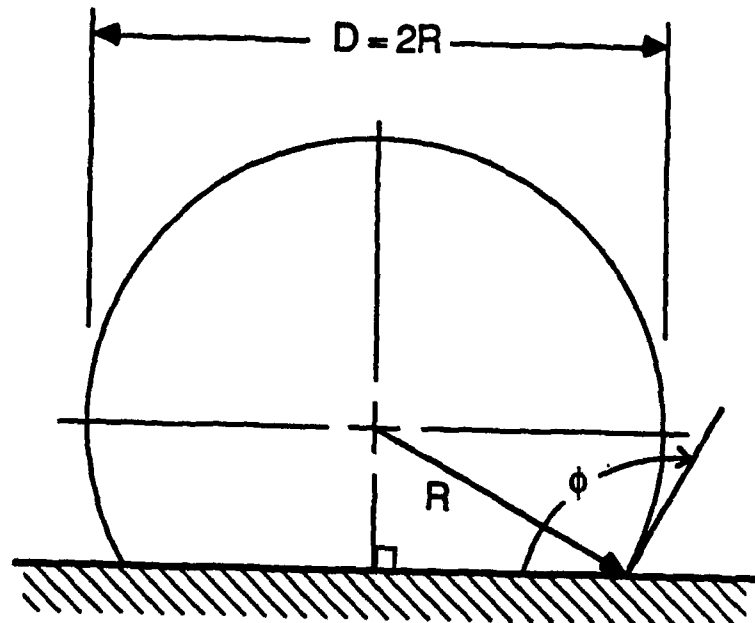
Figure 6.2.2: Droplet measurement geometry

The droplet velocity measurements are area averaged. Using mass conservation of air and water flow through the air nozzle exit, average droplet velocities were calculated. This method provides a total area averaged velocity which does not individually consider the momentum of the air or water flow fields. Hence, the droplet velocity is underestimated; however, it lends insight and material for analysis.

Table 6.2.1 shows the results of these measurements for four different cases. These cases will be used to describe the experimental results presented later. Comparison of these droplet diameter and velocity ranges with the ideal range curve presented earlier indicates that the spray characteristics fall near the entrainment line. This was expected since the method of accelerating the droplets relies on entraining them in the air stream. This indicates that the CHF will be reached when the liquid supply becomes deficient because of entrainment in the escaping vapor.

Table 6.2.1: Experimental flow field parameters

Case	Water Flow Rate l/hr	Drop Size Average/Range μm	Average Velocity m/s	Air Pressure /Flow Rate psig, l/hr
1	2.5	131/ 68 - 219	6.0	20 / 584
2	2.5	108/ 73 - 158	7.5	30 / 739
3	2.5	85/ 42 - 155	9.3	40 / 890
4	3.7	114/ 59 - 200	9.3	40 / 890

6.2.2 Water and Air Flow rate Calibration

With the aid of a variable flow gear pump, orifice plate flow meter and a differential pressure transducer, we calibrated the flow rate versus pressure difference over a range of 0.2 cc/s to 2 cc/s. Similarly, for a fixed jet size on the Paasche Air brush, we calibrated the absolute air pressure to air flow rate using a wet test meter, over the range of 0 to 60 psi, which corresponds to 0 to 350 cc/s.

6.3 RESULTS AND DISCUSSION

We conducted a fixed set of experiments to study the effect of liquid/gas flow rate, droplet size/velocity, and sensible heat content of the liquid on the heat transfer rate at surface temperatures below the Leidenfrost point. All comparisons are in the form of total heat flux versus the surface temperature.

Prior to spraying the surface with droplets, we measured the contribution of the air jet to the heat flux. Even though the flow

field with the droplets is more complex, the heat dissipation solely due to air was 17 W/cm² at a surface temperature of 100 °C, comparatively negligible.

A heated surface of 1 cm² circular cross section was fabricated as described in the experimental section. The whole heater body and thermocouple leads were well insulated with Fiberfrax ceramic fiber insulation, which maintains its low thermal conductivity (approximately 0.1 W/m °K) at high temperatures. This is then placed in an aluminum box, from which the power leads for the lamps and thermocouples are accessed, and compressed air for cooling the lamp ends is injected. The whole assembly is then covered with aluminum foil, such that only the cooled test surface is exposed to the coolant.

Before each experiment, the test surface is cleaned lightly with 1/0 emery polishing paper, then swabbed with hydrochloric acid and finally washed with deionized distilled water. Freshly, deionized distilled water is used as the coolant in all experiments. Experiments were performed with the spray nozzle approximately 23 mm above the surface. In such a position, the whole surface received the spray evenly, and most of the liquid impinged on the surface before being swept away by the air flow. The liquid and air flow rates were monitored at preset rates throughout each experiment.

Experiments were begun at room temperature and ramped up continuously until Leidenfrost conditions were reached, after which the heaters were automatically shut off and the recorded data analyzed. After cooling down, the surface was prepared again for the next run. An immediate rerun or cooling cycle data is not taken, as after the temperature jump to Leidenfrost conditions; a thin layer of oxide forms on the surface, thus changing its characteristics. A copper surface was selected because of its high thermal conductivity and wettability with water, an important parameter in film boiling/evaporation.

Table 6.2.1 provides the parameters of the flow field for four different cases of liquid flow, gas flow and liquid temperature measured at nozzle exit. A number of experiments were performed to check for repeatability, occurrence and value of the critical heat flux (CHF). The repeatability of the experiments is very good lying well within 3 percent of the heat flux at any temperature. However, determination of

the CHF point exactly, is beyond the means of this heater-block system.
In the CHF region, the flow at the surface tends to shift back and forth
between the wetting and nonwetting regions. At this juncture,
temperature shifts range from 120 °C to 140 °C. The copper block system
has a thermal capacity of approximately 850 J/°C, which means, in the
CHF region, where heat flux rates are of the same magnitude or higher,
it takes a second for every degree drop. However, the surface
temperature fluctuates at a much higher rate. Hence, if the surface
flow condition changes to an adverse film boiling situation, then the
heat flux will drop, which exacerbates the problem further, driving the
surface temperature even higher, thus having a run-away effect leading
to the Leidenfrost point.

Figure 6.3.1 compares the change in heat flux with increasing
droplet velocity for the same liquid flow rate (see Table 6.2.1). The
water temperature in both cases is 28 °C. Here we note the cold water
has a significant effect in the subcooled region. At 98 °C, the slope
changes sharply; as phase change begins, the heat flux increases at the
rate of 16 W/°C superheat. At about 107 °C, the slope reverts and
starts decreasing gradually, and near the CHF point (about 130 °C to 135
°C), a maximum is noted. We note no appreciable change in the heat flux
due to change in velocity until this region is approached. This is
because the surface is kept equally wet in all three cases for the lower
heat fluxes. However, in the region of the CHF, we observed higher heat
removal rates with the higher velocity drops. This is because the vapor
evolution entrains the slower droplets, preventing them from reaching
the surface. Hence, the cases in which the droplets have higher
momentum result in higher heat flux. Flow visualization indicates a
more even distribution of droplet size at the higher velocities. At
lower velocities, larger droplets exist and may reach the surface, but
their numbers are insufficient to sustain higher heat flux rates. These
experiments indicate an increase in the critical heat flux with velocity
at a constant flow rate, the increase being about 3 percent between case
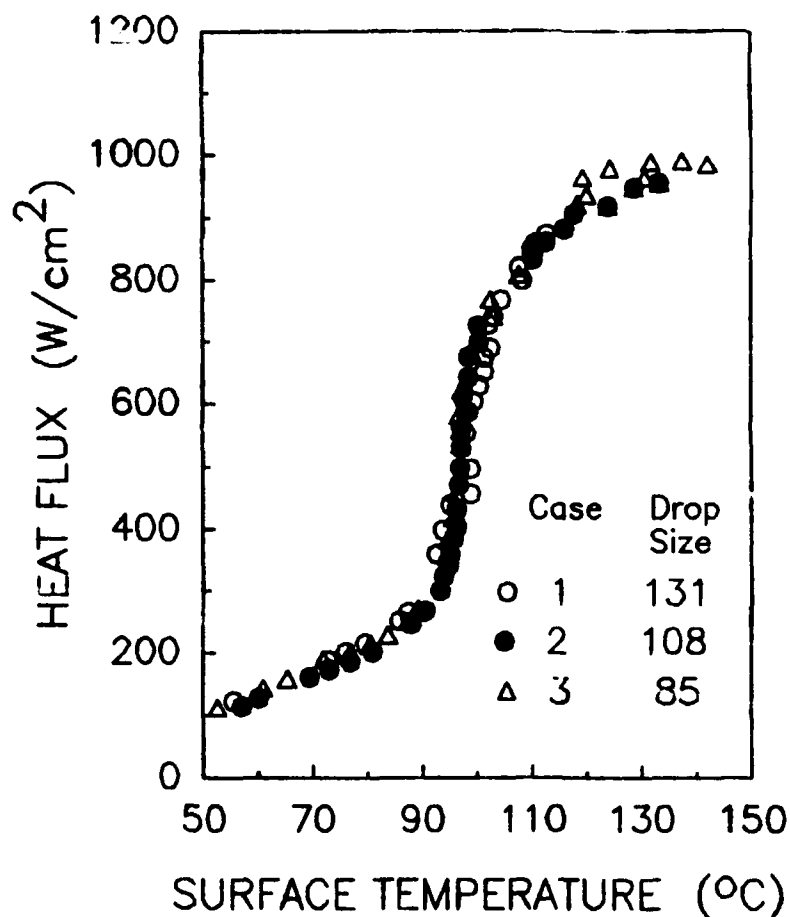2 and 3.

Case	Drop Size
○ 1	131
● 2	108
△ 3	85

Figure 6.3.1: <u>Heat flux vs superheat, drop size effects</u>

Figure 6.3.2 compares the effect of cold water (31 ^{0}C), versus hot water (81 ^{0}C), on the heat flux for case 4. Below saturated conditions, 100 ^{0}C, the cold water has a significantly higher heat removal rate than the hot water. Once saturated conditions are reached, both show identical trends. This is because, as explained earlier (Figure 6.3.1), in this region, the liquid required on the surface is sufficient in both flow fields to remove the given heat flux. However, on reaching the CHF region, the hot water provides much higher heat flux rates. At such high heat flux rates experienced in this region, the drop of water impinging the surface must have as short a residence time in heat removal, going from subcooled to saturated to vapor. The hot water is almost at saturated conditions when it impinges the surfaces, and hence, removes heat through phase change almost immediately. The cold drop on

making contact with the surface, must heat to saturation before
evaporation. Water has a low thermal conductivity, hence the surface on
the impacting side will vaporize immediately before the rest of the drop
can be raised to saturated conditions, the evolving vapor tending to
lift/fold the liquid film, suspending/entraining it. Thus the liquid is
impeded from reaching the surface, which causes the surface temperature
to rise, leading to deterioration in the heat flux conditions. In this
case the maximum heat flux attained was 1,180 W/cm² for the hot water,
and 1,040 W/cm² for the cold. At this flow rate and CHF, 1.95 times the
required quantity of water was sprayed on the surface. The excess
liquid supply is most probably entrained in the escaping vapor and swept
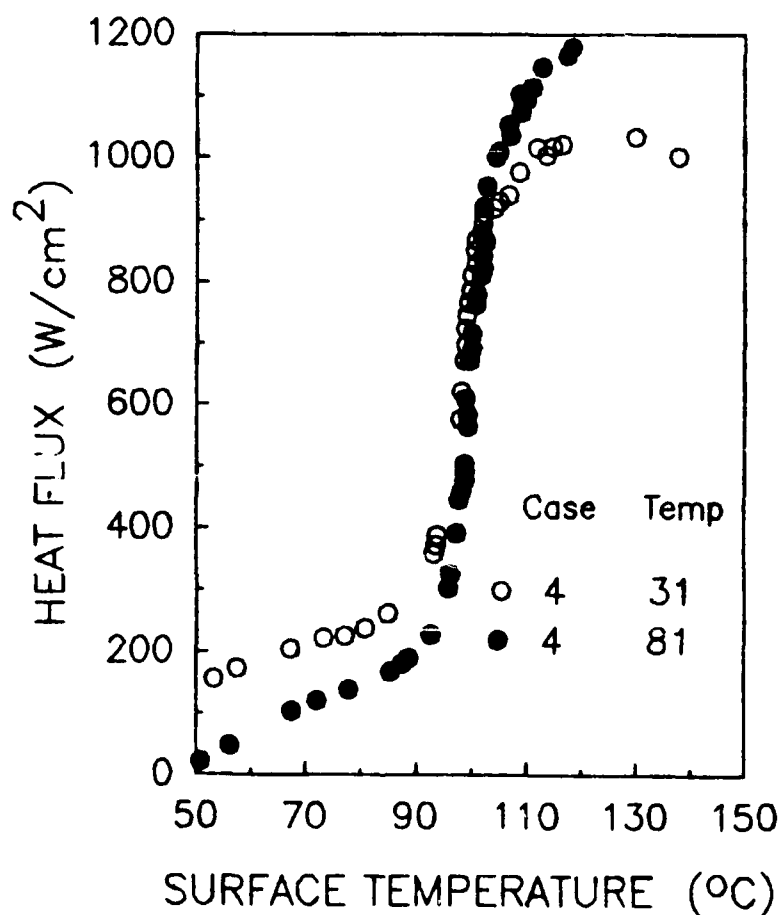away by the stagnation flow field.

Figure 6.3.2: Heat flux vs. superheat, preheat effects

Figure 6.3.3 again compares the change in heat flux for water temperatures of 28 °C and 81 °C with flow conditions specified by case 3. In this case we observed no significant change. This is because the flow rate is very near (1.5 times) that required for heat removal, some of the flow being swept away by the stagnation air flow, rebound and entrainment. Therefore, the CHF is reached because of deficient liquid supply before the effect described above becomes significant. In this case, a heat flux of 1,000 W/cm² was attained in each case.

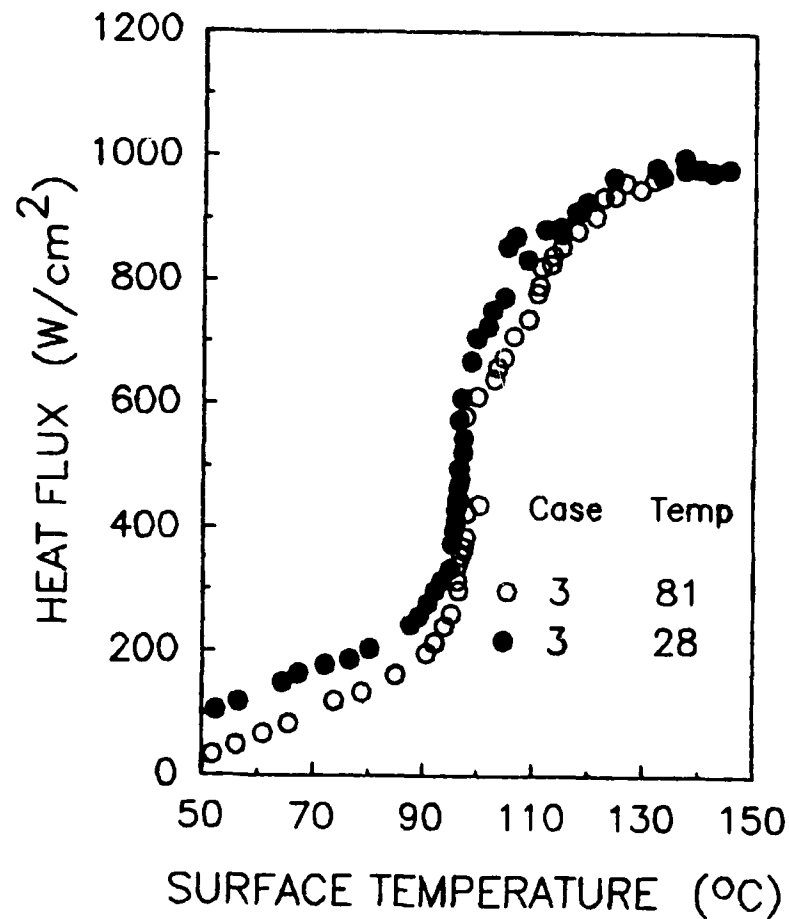| Case	Temp
o 3	81
● 3	28

Figure 6.3.3: Heat flux vs. superheat, preheat effects

Figure 6.3.4 shows the effect of the change in flow rate (cases 3 and 4) on the heat flux, at an initial water temperature of 28 °C. The higher flow rate removes 15 percent more heat in the unsaturated region, having identical values in the nucleate boiling region. In the CHF region, it removes 6 percent more heat for the same degree of superheat. Experiments performed at flow rates well above 3.7 liters/hr do not show appreciable increases in heat flux. This would imply that the flow rate in case 3 is not optimum for maximum heat removal.
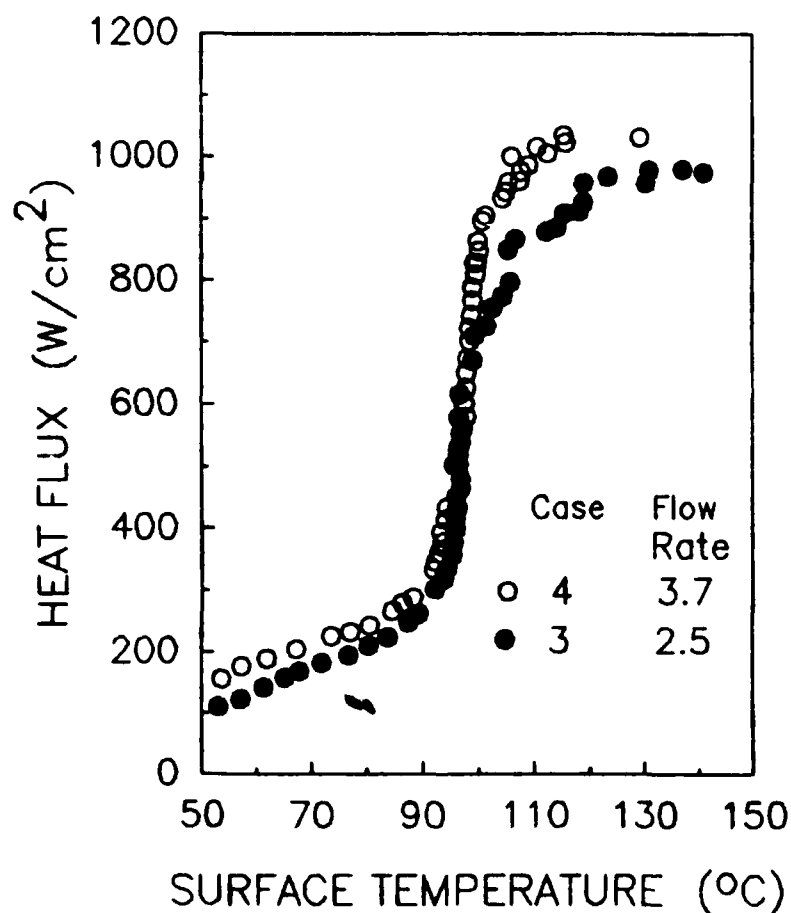

Figure 6.3.4: **Heat flux vs. superheat, flow rate effects**

In all these cases, an abrupt break in the heat flux curve occurs near the CHF because the thermal inertia of the copper block does not permit instant temperature retardation, hence, run away conditions predominate.

6.3.1 Additional Experiments

Additional experiments were performed with the pressure atomizing nozzles used for the preliminary experiments. As mentioned previously, the spray characteristics are not well suited for efficient cooling. The liquid flow rates are too high, and the droplet diameters and velocities are too large. However, two cases are presented here in which the distance between the nozzle and the test surface was increased from 1.9 to 2.5 cm to reduce the amount of coolant striking the surface and to decrease the impact momentum of the droplets. These two cases for nozzles 1 and 2 in Table 5.1.1 were conducted for a pressure of 20 psig. The results are presented in Figure 6.3.5. The results show a slight increase in the CHF and a large improvement in heat transfer efficiency as compared to the nozzle 1 and 2 cases in Figure 4.2.1. The surface temperature at the maximum heat flux is reduced by approximately 15 ^{0}C for each case. The reason for the improvement is that the subcooled region (region I) discussed previously is eliminated by the reduction in total flow rate. As soon as the surface temperature approaches 100 ^{0}C, the more efficient evaporation heat transfer (region II) begins. The results obtained with the new apparatus also show better repeatability than was possible using the preliminary apparatus. This is because the temperature control capability made it easier to perform each run in the same manner. Two runs are shown for each case in the figure.
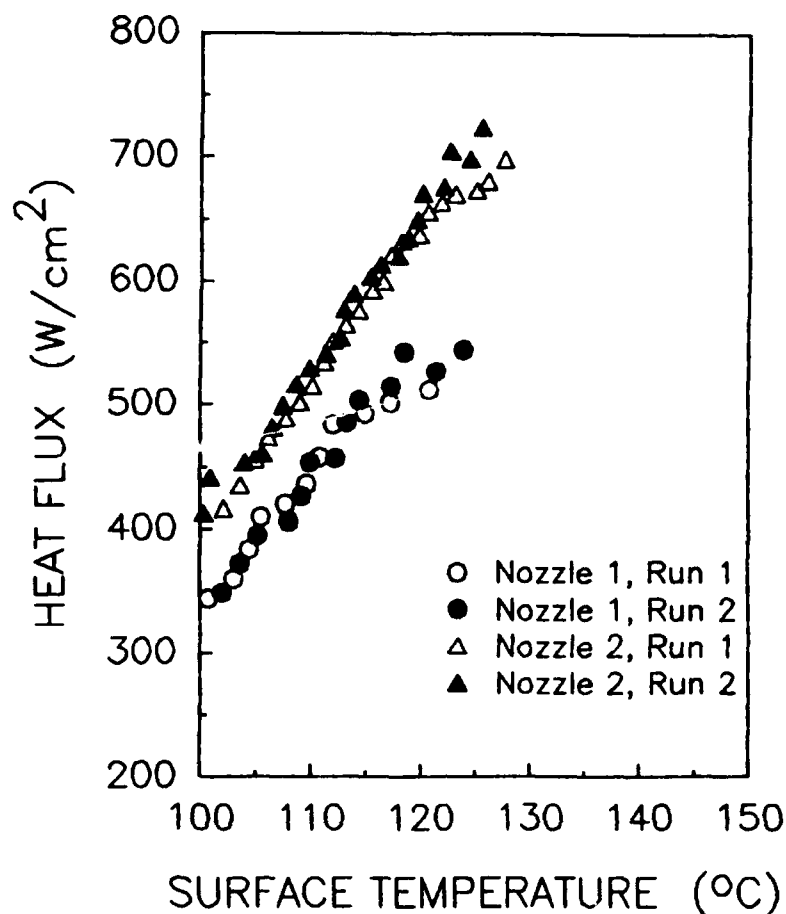
Figure 6.3.5: **Heat flux vs. superheat, pressure fed nozzles**

6.4 RESULTS COMPARISON

This section compares the present experimental results to those previously published. The critical heat flux values are much higher than those obtained by Toda [1]. Toda used a volume flow rate of about 1 gph or less. Droplet velocities and droplet sizes were on the order of 50 m/s and 200 μm, respectively. These give much greater Weber numbers compared to the present experiment and consequently more droplet rebound, resulting in a liquid deficiency at a much lower heat flux. We believe that the maximum heat flux for these cases was governed by a deficiency in liquid supply due to droplet rebound. Bonacina et al. supplied low volume flow rates of about 1-2 gph using droplets of small diameter and low velocity [3]. The overall flow rate was sufficient to

remove a very high heat flux. However, only a small percentage of the coolant impinged upon the surface. The droplet velocities and droplet sizes were approximately 1-2 m/s and 50-100 μm, respectively. The heat transfer coefficients they obtained were moderate due to the low percentages of surface saturation. The maximum heat flux removed was about 200 W/cm^2. They speculated that much larger heat fluxes could have been obtained. However, this was not investigated due to apparatus limitations. No droplet rebound or excess liquid buildup was observed on the surface for these cases. Analysis of the spray conditions for this research indicates that at higher heat fluxes, the droplet diameters and velocities would have to be increased to avoid entrainment in the escaping vapor. Eastman and Ernst obtained very high heat fluxes [2]. However, the heat transfer coefficients were very low. For a heat flux of 1,000 W/cm^2, the preliminary experiments yielded a surface superheat of only 45 ^{0}C, and the improved experiments only 5 ^{0}C, while Eastman and Ernst obtained superheats of over 100 ^{0}C. The reason for this difference is not readily apparent since no data concerning spray conditions is known for the Eastman and Ernst experiments. However, in general it appears that the lower the overall flow rate, the lower the superheat. This is expected because the lower flow rates will yield thinner liquid films which provide more efficient heat transfer.

The experiments conducted with the new apparatus and the previous pressure atomizing nozzles also support the hypotheses presented in this report. The reduced liquid flow rate impinging on the surface resulted in much more efficient heat transfer. Increasing the distance between the nozzle and the surface decreased the liquid supply to the surface, but decreased the droplet impact momentum, resulting in much less droplet rebound. The net effect was a slight improvement in CHF.

Once again, the importance of choosing the proper spray characteristics is apparent from the results comparison. Even though the spray conditions provided by the improved experiments are not ideal, they represent a tremendous improvement in heat transfer efficiency. Since much less droplet rebound occurred than in the preliminary experiments, reductions in overall flow rate in excess of 80 percent were possible for any given heat flux. At the same time, heat transfer

efficiency increased dramatically. At maximum CHF of 1,180 W/cm^2, the improved experiments reduced the surface temperature by nearly 50 ^{0}C. Apparently the CHF limitations approached in the improved experiments were dictated by a liquid deficiency resulting from droplet entrainment. This was, of course, expected since the mechanism of droplet acceleration towards the surface was entrainment in the air stagnation flow field. As the heat flux increases, the increased vapor evolution from the surface causes a change in the stagnation flow field that results in a greater percentage of the spray being swept away from the surface.

VII CONCLUSIONS AND RECOMMENDATIONS

We conclude that the spray characteristics govern the heat transfer process for this type of high power density evaporative cooling. Just as in pool boiling, the interaction between the liquid and the vapor has a significant effect on the critical heat flux. Evidence of these limits is seen in the analysis of the experimental results. The spray characteristics in the preliminary experiments were such the the CHF was dictated predominantly by droplet disintegration and rebound. Conversely, the spray characteristics in the improved experiments were such that droplet entrainment led to the CHF. However, spray characteristics can be chosen for a given heat flux such that the droplet diameters and velocities are in a range which avoids undesirable droplet disintegration and rebound and entrainment. This will allow the volume flux to be more closely matched to the heat removal requirements thus limiting the excess liquid present. Experimental results have shown that this will improve heat transfer efficiency by reducing the liquid film thickness on the surface.

The analytical model results suggest that if the spray conditions are varied within the ideal range, greater improvements in heat transfer efficiency can be obtained by using the smallest possible droplets and the highest percentages of surface saturation. These conclusions are also supported by experimental data.

We have shown that accurate measurements of the spray characteristics can indeed give good predictions of the maximum possible heat flux for a given set of spray conditions. We recommend that a technique for accurately controlling the droplet diameters and velocities and surface saturation be developed so that the optimum conditions within the suitable range can be accurately identified. In addition to the spray characteristics, the surface saturation conditions and the liquid film thicknesses also need to be accurately measured before accurate predictions of heat transfer coefficients and surface superheats can be made.

We also recommend that a method for protecting the surface from degradation be developed to ensure the uniformity of the wetting

characteristics. A surface which wets well and is resistant to oxidation will increase the heat transfer efficiency by providing thinner liquid layers.

REFERENCES

1. Toda, S., "A Study of Mist Cooling," Heat Transfer-Japanese Research, Vol. 1 (3), 1972, pp. 39-50.

2. Eastman, G.Y., Ernst, D.M., "High Power Density Evaporative Cooling (HIPDEC)," Final Report, Air Force Weapons Laboratory, Kirtland AFB. September, 1982.

3. Bonacina, C., Del Guidice, S., Comini, G., "Dropwise Evaporation," Journal of Heat Transfer, Vol. 101, August 1979, pp. 441-446.

4. Vennard, J.K. and Street, R.L., Elementary Fluid Mechanics, 6th ed., John Wiley & Sons.

5. Callen, H.B., Thermodynamics, John Wiley & Sons, 1960.

6. Dufour, L. and Defay, R., "Thermodynamics of Clouds", International Geophysical Series, Vol 6, Academic Press, 1963.

7. Thomson, J.J., Application of Dynamics, London, 1888.

8. Thomson, W., Phil. Mag., 4th Series, Vol 42, pg 448, 1871.

9. Guggenheim, E.A., Thermodynamics, An Advanced Treatment for Chemists and Physicists, 3rd ed., North-Holland, 1957.

10. Guggenheim, E.A., Mixtures, The Theory of the Equilibrium Properties of some Simple Classes of Mixtures Solutions and Alloys, Clarendon Press, 1952.

11. Harkins, W.D., Physical Chemistry of Surface Films, Reinhold Publishing Corp., 1952.

12. Frenkel, J., Kinetic Theory of Liquids, Clarendon Press, 1946.

13. Collier, J.G., _Convective Boiling and Condensation_, Mcgraw Hill, 2nd ed., 1981.

14. Bankoff, S.G., _Ebullition from Solid Surfaces in the Absence of Preexisting Gaseous Phase_, Trans. ASME, 79, pg 735, 1957.

15. Zuber, N., _Nucleate Boiling - the Region of Isolated Bubbles - Similarity with Natural Convection_, Int. J. of HT, 84, pg 204, 1962.

16. Bachelo, W.D., and Houser, M.J., "Development of the Phase/Doppler Spray Analyzer for Liquid Drop Size and Velocity Characterization," AIAA Paper No. AIAA-84-1199, 20th Joint Propulsion Conference, Cincinnati, Ohio, June, 1984.

17. Wachters, L. and Westerling, N., "Heat Transfer from a Hot Wall to Impinging Water Droplets in the Spheroidal State," _Chemical Engineering Science_, Vol. 21, 1966, pp. 1231-1238.

18. Rizza, J.J., "A Numerical Solution to Dropwise Evaporation," _Journal of Heat Transfer_, Vol. 103, 1981, pp. 501-507.

19. Ames, W.F., _Numerical Methods for Partial Differential Equations_, Barnes & Noble, New York, 1969.

20. _Manual on the Use of Thermocouples in Temperature Measurement_, ASTM Special Publication 470A, Omega Press, Stamford, CT 06907, 1974.

21. Schlichting, H., _Boundary Layer Theory_, Mcgraw Hill.